POLITECNICO DI TORINO

Master of Science in Mechatronics Engineering

Politecnico di Torino

Master of Science Thesis

Data-based Modelling of Nonlinear Hydrodynamics for Wave Energy Conversion Systems

Supervisors

Prof. Nicolas FAEDO

Prof. Giuseppe GIORGI

Candidate

Ruoqing ZHU

April 2024

Summary

This thesis explores the intricacies of data-based modeling for nonlinear hydrodynamics in wave energy conversion systems. It explores into the complexities of wave energy conversion, highlighting the need for precise and computationally light modeling to be prepared for control design phase to optimize system performance. Through the development of a two-degree-of-freedom model integrating nonlinear Froude-Krylov effect, the thesis aims to deepen our understanding of wave energy converters and contribute to the advancement of more effective technologies in the field. The thesis presented here could offer insights for the wave energy conversion systems, suggesting how data-based modeling can contribute system efficiency and reliability. In essence, this thesis represents a modest yet meaningful contribution to the field of wave energy conversion, laying groundwork for further research and development in sustainable energy technology.

Acknowledgements

I am profoundly grateful to my supervisor, Professor Nicolas Faedo and Professor Giuseppe Giorgi, for their invaluable guidance, patience, and support throughout the course of this research.

I am immensely thankful to my family, who have supported me emotionally and financially through my entire academic journey. Without their unconditional belief in my abilities, this thesis would not have been possible.

As I mark the end of my time at Politecnico di Torino, I look back with fondness on the experiences that shaped who I am today. This thesis not only represents a culmination of my academic endeavors but also a significant personal milestone. My time at Politecnico di Torino has been a period of immense growth and self-discovery, and I am grateful to all my friends who have been part of this journey.

Ruoqing Zhu

Table of Contents

List of Tables

List of Figures

Acronyms

WEC
: wave energy converter

DoF
: degree of freedom

FK
: Froude-Krylov

BEM
: boundary element method

NWT
: numerical water tank

EFTE
: empirical transfer function estimation

Chapter 1

Introduction

1.1 Background

Wave energy gives a substantial and reliably predictable form of renewable energy, with abundent potential resources(estimated total wave energy is up to 80,000 TWh a year[1]). The extraction of wave energy from oceans holds the promise of making significant contributions to global sustainability objectives, aligning with the pursuit of a better environment on earth. So wave energy converter systems have emerged to make use of the vast renewable energy hidden in the ocean waves. These systems are designed to capture the kinetic energy and potential energy present in waves and convert it into electrical power.

Wave energy Convertors (WEC) of different mechanisms have been implemented to extract energy from shoreline out to the deeper water offshore to harness wave energy efficiently. The most common ones are: attenuator(floating devices capturing energy from the relative motion of the two arms), point absoeber(converting the motion of the buoyant top relative to the base into electricity), oscilating wave surge converter(extracting energy from wave surges and the movement of water particles within them), oscilating water column(generating electricity through airflow by waves compressing and decompressing the air in a hollow structure), overtopping/terminator device(waves breaking into a reservoir, then returning to the sea through a low-head turbine to generate power), submerged pressure differential(waves causing alternating pressure thus pumping fluid through a system to generate electricity), bulge wave(water passing a mooring rubber tube filled with water to generate power via pressure variation), rotating mass(capturing electricity by the movement of the device heaving and swaying in the waves)[2].
While the specific configurations and operational principles vary among these devices, the most fundamental principle of absorbing energy from ocean waves

involves intricate interactions between the mechanical components of WECs and the dynamic motion of the waves themselves. Understanding the principle is essential for optimizing the design and performance of WEC systems. The mechanisms of WECs commonly used mentioned before can be broadly categorized into three types:

- Hydrodynamic Effects: utilizing the pressure differentials and fluid dynamics induced by wave motion.
- Mechanical Oscillation: relying on mechanical oscillation induced by wave action to capture energy.
- Wave-Structure Interaction: harnessing the relative motion between waves and fixed or floating physical structure of WECs to extract energy through mechanisms such as pitch, heave, or surge motion.

However, it should be noted that wave energy technology is still in its early stages of development compared to other renewable energy such as solar and wind energy. As a result, currently it is not competitive commercially when compared to traditional fossil fuel or nuclear energy. The primary reason hindering commercialization is inefficient energy extraction usually due to the fact that the WEC's dynamic parameters are not optimally tuned thus their control is not optimal for most wave profiles[3]. And the irregular and stochastic nature of ocean waves brings significant challenges for WEC's dynamic parameters tuning. Also WEC have to confront with the disadvantage of wave power, which is the significantly random variability in several timescales: from wave to wave, with sea state, and from month to month[4].
Control technology plays a critical role in addressing these challenges of optimizing the operation of WECs in real-time. Through advanced control technology, WECs can adapt their response to changing wave conditions, ensuring maximum energy absorption under diverse environmental scenarios.

1.2 Motivation

To optimize the energy extraction from ocean waves using wave energy converters (WECs), it is necessary to design a more effective controller. To advance the design of a sophisticated controller, there are several key motivations drive us to come up with a new modelling approaches:

1. The operational range of motion for wave energy converters can extend into nonlinear regimes, where the interaction between the device and wave forces becomes increasingly complex. Nonlinearities arise from various sources, including fluid-structure interactions and hydrodynamic effects. These nonlinear

effects can manifest as phenomena such as wave-induced motion, resonance amplification, and energy dissipation[5].
As the operational envelope of WECs expands to accommodate a wider range of wave conditions and operating scenarios, the significance of nonlinear dynamics becomes more pronounced. Failure to adequately account for these nonlinear effects in WEC modeling can lead to inaccurate predictions of device performance, compromising design optimization efforts and hindering the development of effective control strategies. Among all the sources of nonlinearities, Froude-Krylov (FK) effect, which play a crucial role in the energy absorption performance of WEC systems[6].

2. The complexity of wave energy converter models presents challenges in terms of computational effort. The ratio bettween accuracy gain and computational effort is descreasing as the model get more complicated in terms of intricate geometries, control strategies, and environmental considerations. So nowadays the engineering challenges to WEC design include the trade-offs in modeling accuracy versus computational cost[7]. And real-time feasibility is essential in wave energy converters for two reasons:

   - Real-time control: Real-time feasibility is necessary to implement control strategies that can adjust the WEC's behavior based on changing wave conditions and other factors to optimize their performance and ensure safe operation.
   - Real-time simulations: Real-time simulations are used to test and validate WEC in the design stage. Real-time feasibility is essential to ensure that simulations can be completed quickly enough to provide useful feedback for design and control optimization.

   The computational demands of WEC models can be significant due to factors like the radiation convolution integral. These challenges highlight the need to balance modeling accuracy with computational efficiency, especially when considering real-time applications[8].

3. While the majority of wave energy converter control strategies primarily focus on linear hydrodynamic WEC models (as evidenced in sources such as[9]), exceptions do exist. These exceptions mostly involve the consideration of relatively 'simple' nonlinear hydrodynamic effects, in terms of analytical complexity. For instance, some studies have investigated the incorporation of nonlinear effects such as viscous drag forces and state-dependent restoring effects[10]. These efforts signify a departure from the conventional linear models and reflect a growing interest in understanding and harnessing the nonlinear dynamics inherent in wave energy conversion systems. But as

mentioned before, the Froude-Krylov (FK) effect is a significant nonlinear contribution to the hydrodynamic force experienced by a variety of wave energy converters (WECs) currently in development[6].
The Froude-Krylov (FK) effect is a nonlinear hydrodynamic force that results from the pressure distribution on the WEC surface due to the incident waves. The nonlinearity of FK effect is more significant in devices with variable cross-sectional areas due the fact that the variable cross-sectional area can cause complex pressure distributions on structure surface. And recent WEC design trends are moving towards floating structures with variable cross-sectional areas, thus it is important to consider nonlineaar Froude-Krylov effect.

4. There are some papers take the nonlinear Froud-Krylov effect into consideration, such as a variable-structure control strategy developed for a heaving point absorber WEC to handle both static and dynamic Froude-Krylov forces[11]. Similarly, a nonlinear model predictive controller for a WEC system with comparable dynamic characteristics is designed to handle this[12]. However, both strategies outlined before share a fundamental drawback: they rely on an analytical model that represents Froud-Krykov effects, particularly dynamic part of it, assuming a regular (monochromatic) free-surface elevation, which is composed of a single frequency component. But this is a strong assumption, as real ocean waves are typically panchromatic, meaning they are composed of a range of frequencies. The limitation of this assumption is that it may not accurately represent the complex dynamics of real-world wave conditions, which can have a significant impact on the performance of WECs. Therefore, the controllers developed using these models may not be directly applicable in realistic scenarios, where the ocean wave conditions are more complex and varied.
   Not only due to the poorly representation of real world, but also due to the reason that with those models, wave number which can only be defined for regular wave inputs is necessary for design and synthesis procedure of control technology. Consequently, the application to stochastic (irregular) wave fields is not available.
   Another similar issue is that this assumption is also used to derive a closed-form expression for the latching time, which is necessary for the implementation of latching control in heaving WEC systems such as [13][14].
   This highlights the need for more sophisticated models that can accurately represent the complex dynamics of real-world wave conditions and the nonlinear Froude-Krylov effects that arise from them.

5. Model-based control strategies play a crucial role in optimizing the performance of WECs by regulating device operation in response to varying environmental conditions and operational objectives. The absence of a model-based optimal

control design for WEC systems, taking into account nonlinear Froude-Krylov (FK) effects, may contribute to the lack of control-oriented models that accurately capture these effects in a way that aligns with contemporary control methods.
Numerical methods, such as the analytical method, boundary-integral equation method, Navier-Stokes equations method, and empirical method, have been used to model floating-point absorbers in wave energy converters. However, the utility of those models for control design could be constrained by computational limitations, model inaccuracies, and the complexity of WEC dynamics. For instance, the analytical method assumes a linear relationship between the wave height and the wave velocity, which may not hold in real-world scenarios where that can be nonlinear. Similarly, the boundary-integral equation method assumes that the fluid is not viscid and not compressible, which may not be true in real-world scenarios[15]. Regardless of the inaccuraccy and computation limitation of those models, numerical methods like NLFK4ALL developed by Giorgi[16] could hardly used for control techniques design. Because this method assumes a 'frequency-by-frequency' decomposition of the pressure field, which does not align well with model-based control design requirements. Model-based control synthesis typically necessitates a closed-form description, at least in terms of input-output dynamics[10].
Developing control-oriented models could offer a promising alternative for model-based control strategies, at the same time, providing a computationally efficient framework for capturing the essential dynamics of WEC systems while accommodating uncertainties and nonlinearities.

In light of these listed motivations, the pursuit of developing control-oriented models stands as a promising way to designing highly effective model-based control strategies. By focusing on the complicated dynamics of WEC systems, such models have the potential to accurately capture system behavior while maintaining computational efficiency. Moreover, they enable the accommodation of uncertainties and nonlinearities inherent in real-world wave energy conversion scenarios.

1.3 Objective

A control-oriented model is a mathematical representation of a system that is used to design and analyze control systems. A control-oriented model is different from traditional models by emphasizing the representation of system dynamics in a form that is conducive to control design and analysis. It is a simplified model of the system that focuses on the aspects that are relevant for control design, such as the system's dynamics and response to inputs. A control-oriented model should be able to predict the system's behavior accurately enough for control design

purposes, while being computationally efficient and easy to manipulate. A good control-oriented model should have the capability to predict observed data and be represented in a state-space form that satisfies the separation principle. This principle implies that the future output of the system should depend only on the current state and the future input, with the current state summarizing the effect of past inputs on future outputs.
In the context of wave energy converters, the control-oriented model could be tailored to capture the essential dynamics relevant to control design, such as wave-structure interactions, actuator dynamics, and energy conversion mechanisms. But in this research, nonlinear Froude-Krylov effect which is reason of deficiency of current control systems of WECs. So the primary objective of this research is to develop a control-oriented model for wave energy converters that facilitates the design and implementation of effective control strategies. And it should be a simplified mathematical representation of a system and predict the system's behavior focusing on Froude-Krylov effect accurately enough, while being computationally efficient and easy to manipulate.

To achieve the objective of developing a control-oriented model, this research adopts a data-based framework that make use of the computed data on FK forces and system identification techniques. Specifically, the framework involves:

- Generation of a Set of Froude-Krylov (FK) Data: The first step involves collecting a comprehensive dataset of FK forces under a multinsine wave which encompassing a wide range of frequencies representative of real ocean states. This study will utilize the numerical solver NLFK4ALL to generate this dataset. This dataset serves as the basis for characterizing the hydrodynamic interactions between waves and the WEC structure. By systematically measuring FK forces, a representative dataset is obtained, enabling the identification of key trends and patterns in FK force behavior.

- Model Reduction and System Identification: The device configuration of this study is a giant cylinder which has 6 degrees of freedom. But in order to simplify the complexity of the system by approximating its behavior, a lower-dimensional model which is able to retaine the essential dynamics is developed. And this process is called *model reduction*. In the context of this study, the original 6 degrees of freedom (surge, sway, heave, roll, pitch, roll) is trimed to be 2 degrees of freedom (heave and pitch) to accurately capture the physics of a system in terms of our interest in a wave energy converter.
  System identification is a methodology for building mathematical models of dynamic systems using measurements of the system's input and output signals which is dataset from NLFK4ALL solver in this study. Through

this process, the control-oriented model is created to capture the dominant dynamics governing WEC performance, facilitating the design of effective control strategies.
In this study, two separate models will be developed to accurately represent static Froude-Krylov effects and dynamic Froude-Krylov effects.

Chapter 2

Theoretical Preliminary

2.1 Frequency-Domain Models

In the numerical modeling of Wave Energy Converters (WECs), the application of Newton's second law is essential, asserting that the net force acting on the WEC is balanced by the total forces applied. These forces include:

- *Hydrostatic force* This results from changes in the hydrostatic pressure distribution due to the device's oscillatory movements.
- *Excitation loads* These are generated by the interaction of incident waves with the stationary device.
- *Radiation force* This arises when the device alters the surrounding pressure field through its own oscillations, in the absence of external wave activity.

2.1.1 Potential Flow Theory

Potential flow theory assumes ideal flow conditions, characterized by inviscid (frictionless) and irrotational fluid motion. In inviscid flow, there are no viscous shear stresses, only normal stresses are present, and fluid elements do not deform or rotate. Irrotational flow means that fluid elements do not rotate relative to their center of gravity.

1. **Laplace Equation**
   If we assume the flow to be in-compressible, the continuity equation becomes:

$$\nabla u = 0, \tag{2.1}$$

   where $u(x, y, z)$denotes the fluid velocity vector and x, y and z z represent the spatial coordinates in a three-dimensional space, with x being the direction

of the wave, z indicating the up and down direction, and y representing the remaining spatial direction, in a right-hand coordinate frame.
Since potential flow theory assumes the flow is irrotational, the curl of u is zero:

$$\nabla \times u = 0 \tag{2.2}$$

The water velocity can be also expressed in terms of a velocity potential, $\phi(x, y, z, t)$:

$$u = \nabla\phi \tag{2.3}$$

By combining these equations, Laplace Equation is formulated:

$$\nabla^2\phi = 0. \tag{2.4}$$

2. **Boundary Conditions**
Dynamic boundary conditions arise from maintaining pressure stability at the fluid's free surface. Leveraging the Bernoulli principle, which describes fluid dynamics and energy preservation, these conditions can be effectively integrated at the free surface to consider the boundary conditions.

$$\frac{\partial\phi}{\partial t} + \frac{1}{2}(\nabla\phi)^2 + g\eta = 0 \text{ on } z = -\eta(x, y, t) \tag{2.5}$$

where η represents the deviation of the water's free surface from its resting state, with positive values indicating that the surface is raised above the xy plane.

Kinematic boundary condition requires that the component of the fluid velocity normal to the surface must equal to the surface velocity:

$$\frac{\partial\eta}{\partial t} + \frac{\partial\phi}{\partial x}\frac{\partial\eta}{\partial x} + \frac{\partial\phi}{\partial y}\frac{\partial\eta}{\partial y} + \frac{\partial\phi}{\partial z} = 0 \quad \text{ on } z = -\eta(x, y, t) \tag{2.6}$$

These two conditions are nonlinear due to the second-order terms but it could be solved by using linear theory based on the assumption that the wavelength is much larger than the wave amplitude. So the second order could be neglected because its magnititude is much smaller than other terms. While applying linear theory, boundary conditions are only considered at the equilibrium position of the free water surface. By ignoring the nonlinear term of them and combining them together:

$$\frac{\partial^2\phi}{\partial t} + g\frac{\partial\phi}{\partial z} = 0 \text{ on } z = 0 \tag{2.7}$$

The boundary condition applied with linear theory over the body-fluid interface requires that fluid velocity component perpendicular to the body's surface, u_n, must equal with the body's velocity in its normal direction:

$$\frac{\partial \phi}{\partial n} = u_n \tag{2.8}$$

The boundary condition at the seafloor requires that there is no vertical component of the fluid velocity, based on the assumption that the seabed is level and located at a depth $z = -h$:

$$\frac{\partial \phi}{\partial z} = 0 \text{ on } z = -h \tag{2.9}$$

Intuitively, at a distance from the oscillatory body, the wave field should remain undisturbed or resemble the incident wave field. So the boundary condition over radiation requires that the magnitude of the potential should diminish proportionally with the inverse of the square root of the distance from the source, reflecting the decay in intensity as distance increases:

$$\phi \propto (kr)^{-1/2} \mathrm{e}^{-\mathrm{i}kr} \text{ as } r \to \infty, \tag{2.10}$$

here r denotes the radial distance from the body and k represents the wave number, related to the wave frequency given by:

$$\frac{\omega^2}{g} = k \tanh kh. \tag{2.11}$$

3. **Decomposition**
To solve boundary value problem, velocity potential could be rewritten as a form of complex amplitude and a sinusoidal time dependence with unit amplitude, $e^{i\omega t}$:

$$\phi(x, y, z, t) = \mathrm{Re}\left\{\hat{\phi}(x, y, z)\mathrm{e}^{\mathrm{i}\omega t}\right\} \tag{2.12}$$

Under the assumption of linearity, the resultant wave field around a WEC can be described as a combination of an incident wave, a diffracted wave, and a radiated wave. In this context, the 'incident field' is characterized by a plane wave propagating freely in the absence of any obstructions. The 'diffracted wave field' emerges due to the interactions between the incident wave and a stationary object. Moreover, the 'radiation wave field' is produced by the oscillations of the object when there are no incoming waves present. Therefore, the total velocity potential can be broken down as follows:

$$\begin{aligned} \phi &= \phi_D + \phi_r \\ \phi_D &= \phi_0 + \phi_s \end{aligned} \tag{2.13}$$

where ϕ_0 and ϕ_s represent the scattered/diffraction and the incident wave potential.
The velocity potential associated with a propagating incident wave is:

$$\begin{aligned}\hat{\phi}_0 &= \frac{\mathrm{i}gA}{\omega} e(kz) \exp\{-\mathrm{i}k(x\cos\beta + y\sin\beta)\} \\ e(kz) &= \frac{\cosh[k(z+h)]}{\cosh kh}\end{aligned} \tag{2.14}$$

where β denotes the angle between the direction of propagation of the incident wave and the x-axis and $e(kz)$ is the decay function where h denotes the water depth, indicating how the dynamic pressure decreases with distance below the still water line.
The scattered wave or diffraction wave is generated by the interaction of the incident wave and the motionless body:

$$-\frac{\partial \hat{\phi}_\mathrm{s}}{\partial n} = \frac{\partial \hat{\phi}_0}{\partial n} \tag{2.15}$$

Here,ϕ_r represents the radiation potential linked with the wave radiated by the body. This potential is required to meet the boundary conditions imposed by the body's oscillations across all unconstrained degrees of freedom. The overall complex amplitude of the radiation potential is determined by the principle of superposition:

$$\hat{\phi}_\mathrm{r} = \mathrm{i}\omega \sum_{j=1}^{N} \hat{\xi}_j \varphi_j \tag{2.16}$$

where N denotes the number of oscillatory modes, $\hat{\xi}_j$ denotes the complex amplitude of the harmonic body motion in mode j and every j indicates a degree of freedom. φ_j is a complex coefficient representing the amplitude of the radiation potential caused by motion in mode j with unit amplitude.

2.1.2 Equation of Motion - single degree of freedom

In the time domain, the general motion equation, based on the second law of Newton, is written as:

$$m\ddot{\xi}(t) = F(t) \tag{2.17}$$

According to linear theory and assuming harmonic oscillations of both waves and the device, it is feasible and advantageous to separate each term of Equation(2.17) into its spatial and temporal components like velocity potential. Therefore, the

device displacement, velocity and acceleration vectors becomes:

$$\begin{aligned}\xi(t) &= \mathrm{Re}\left\{\hat{\xi}(\omega)\mathrm{e}^{\mathrm{i}\omega t}\right\}\\ \dot{\xi}(t) &= \mathrm{Re}\left\{-i\omega\hat{\xi}(\omega)\mathrm{e}^{\mathrm{i}\omega t}\right\}\\ \ddot{\xi}(t) &= \mathrm{Re}\left\{-\omega^2\hat{\xi}(\omega)\mathrm{e}^{\mathrm{i}\omega t}\right\}\end{aligned} \tag{2.18}$$

Hence, the equation of motion may be rewritten as:

$$-\omega^2 m\hat{\xi}(\omega) = \hat{F}_{hd}(\omega) + \hat{F}_{hs}(\omega), \tag{2.19}$$

where $\hat{F}_{hd}(\omega)$ is hydrodynamic force and $\hat{F}_{hs}(\omega)$ id hydrostatic force.

1. **Hydrodynamic Force**
   This force is decomposed into two components: the wave excitation force and the wave radiation force.
   From the Bernoulli equation ignoring second order terms, the dynamic pressure could be written, not considering second-order terms, as

$$p_e = -\rho(\frac{\partial\phi}{\partial t}) \tag{2.20}$$

   Hence, the linear hydrodynamic force of a floating body with wet body surface S_b is obtained from

$$F_{\mathrm{hd}} = \int_{S_{\mathrm{b}}} p_{\mathrm{e}} n dS_{\mathrm{b}} = \rho\int_{S_{\mathrm{b}}} \frac{\partial\phi}{\partial t} n dS_{\mathrm{b}}, \tag{2.21}$$

   As velocity potential is decomposed in Section 2.1.1, hydrodynamic force could be decomposed:

$$\begin{aligned}\hat{F}_{\mathrm{hd}} &= \hat{F}_{\mathrm{e}} + \hat{F}_{\mathrm{r}}\\ &= \mathrm{i}\omega\rho\int_{S_{\mathrm{b}}}\left(\hat{\phi}_0 + \hat{\phi}_{\mathrm{s}}\right) n dS_{\mathrm{b}} - \omega^2\rho\int_{S_{\mathrm{b}}}\sum_{j=1}^{N}\hat{\xi}_j\varphi_j n dS_{\mathrm{b}},\end{aligned} \tag{2.22}$$

   where $\hat{F}_{\mathrm{e}}$ and $\hat{F}_{\mathrm{r}}$ is excitation force and radiation force respectively.

   Excitation Force The wave excitation force on the body is decomposed into two components: the Froude-Krylov force, and the scatter or diffraction excitation force:

$$\hat{F}_{\mathrm{e}} = \hat{F}_{\mathrm{FK}} + \hat{F}_{\mathrm{s}} = \mathrm{i}\omega\rho\int_{S_{\mathrm{b}}}\hat{\varphi}_0 n dS_{\mathrm{b}} + \mathrm{i}\omega\rho\int_{S_{\mathrm{b}}}\hat{\varphi}_{\mathrm{s}} n dS_{\mathrm{b}}. \tag{2.23}$$

The Froude-Krylov force is calculated from the velocity potential of the incident wave which remains unaffected by the presence of the body, resulting from the pressure distribution over the mean wet surface of the motionless body.
The diffraction component of the exciting force came from the integration of the diffraction wave potential on the wet surface. Considering that the Froude-Krylov effect treats the body as transparent, this term serves as a correction factor to account for the presence of the body.

Radiation Force Radiation force arises from the water displacement around the body due to its movement, which may be written as:

$$\begin{aligned} \hat{F}_{\mathrm{r}} &= -\mathrm{i}\omega \mathrm{Z}\hat{\xi} \\ Z &= -\mathrm{i}\omega\rho \int_{S_{\mathrm{b}}} \varphi n dS_{\mathrm{b}} = \mathrm{R} + \mathrm{iX} = \mathrm{R} + \mathrm{i}\omega \mathrm{A} \end{aligned} \tag{2.24}$$

where Z denotes the radiation impedance. R, the real part, signifies the hydrodynamic damping coefficient, accounting for energy dissipation as body oscillations transmit energy to the surrounding water. X, the imaginary part, denotes the radiation reactance, representing the difference between the average kinetic energy added by water displacement and the average gravitational potential energy associated with water surface deformation.
Given the harmonic response of the system, the energy stored in the water oscillates between the mechanical system and the surrounding water and this is the so-called reactive effect. X could be be expressed as ωA, where A denotes the added mass coefficient, reflecting the inertial increase caused by water displaced around the body during motion. Accordingly, radiation force could be rewrite as:

$$\hat{F}_{\mathrm{r}} = -\mathrm{i}\omega R\hat{\xi} + \omega^2 A\hat{\xi}, \tag{2.25}$$

2. **Hydrostatic Force**
The hydrostatic force originates from the balance between buoyancy and gravitational forces. It is determined by integrating the hydrostatic pressure distribution across the body's wet surface under static conditions. For scenarios where the motions of the body amplitudes are very small, a linear approximation of the hydrostatic force can be quite precise. Under these conditions, the hydrostatic force is proportional to the displacement, which simplifies the calculation of its complex amplitude to:

$$\hat{F}_{\mathrm{hs}} = -G\hat{\xi}, \tag{2.26}$$

where G is the hydrostatic spring stiffness and hydrostatic coefficient is another term of it. In the context of a heaving WEC the equilibrium between gravity and buoyancy formulates:

$$G = \rho g S, \tag{2.27}$$

where S indicates the cross-sectional area of body and sea level which is undisturbed. Due to the assumption of linear theory, assuming that this area would be constant during the device moving.

3. **Complex Amplitude of the Body Motion**
   By incorporating the formulated hydrostatic restoring force from Eq. (2.26), alongside the hydrodynamic radiation from Eq. (2.25) and the wave excitation loads from Eq. (2.23) into the equation of motion, Eq. (2.19), after some basic mathematical computation, we derive the complex amplitude of the device motion,

$$\hat{\xi} = \frac{\hat{F}_{\mathrm{e}}}{-\omega^2(m + A) + G + \mathrm{i}\omega R}. \tag{2.28}$$

2.1.3 Equation of Motion - multiple degrees of freedom

The general equation of motion for a multiple degree-of-freedom (DoF) WEC is essentially an expansion of that for a WEC in single DoF as in the last section. It could be easily written in a matrix form as:

$$\hat{\xi} = A_w \hat{\mathbf{f}}_{\mathrm{e}} \left[-\omega^2(\mathbf{M} + \mathbf{A}) + \mathbf{G} + \mathbf{i}\omega\mathbf{R} \right]^{-1} \tag{2.29}$$

where matrix or vector is represented by the bold font denotes. In $\hat{\mathbf{f}}_{\mathrm{e}}$ indicates the vector of complex amplitudes of the excitation wave forces under a unit amplitude wave on the mean body wet surface, and it is usually computed with BEM radiation/diffraction numerical codes such as Nemoh. And other denotations are:

- $\mathbf{M}$ is the mass matrix and for a 2 DoF in terms of heave and pitch of an unconstrained floating rigid body is described by

$$\mathbf{M} = \begin{bmatrix} m & -m x_{\mathrm{g}} \\ -m x_{\mathrm{g}} & I_{22} \end{bmatrix}, \tag{2.30}$$

  where m is the mass of the body, and it equals to the mass of the displaced water under freely floating conditions, given by $m = \rho V$, x_{g} represents the coordinates of the center of gravity, and I_{22} denotes the moments of inertia about the x-axis, related to the corresponding radius of gyration r_{22}, through the relationship:

$$I_{22} = \rho V r_{22} \left| r_{22} \right|. \tag{2.31}$$

- **G** is the matrix of hydrostatic stiffness or hydrostatic restoring coefficients and it is given by:

$$\begin{cases} G_{33} = \rho g \int_{S_\mathrm{b}} n_3 dS_\mathrm{b} \\ G_{35} = -\rho g \int_{S_\mathrm{b}} x n_3 dS_\mathrm{b} \\ G_{55} = \rho g \int_{S_\mathrm{b}} x^2 n_3 dS_\mathrm{b} + \rho g V z_\mathrm{b} - m g z_\mathrm{g} \end{cases} \tag{2.32}$$

- **R** is the damping and **A** is the added mass. As previously discussed, the damping coefficient pertains to the waves generated by the oscillatory motions of the body and the energy dissipated as it is transmitted away from the body. Conversely, the added mass factor addresses the additional inertial effect caused by the displacement of water in the vicinity of the body when it moves, acknowledging that acceleration of a water particle from rest results in acceleration of the surrounding fluid as well. The added mass coefficient comprises two components: a term that dependes on frequency and the infinite added mass. The infinite added mass is a constant that is always positive representing the added inertia at infinite frequency, where no waves are radiated from the body. This constant component is often referred to as $\mathbf{A}_\infty = \lim_{\omega \to \infty} \mathbf{A}$.

2.2 Time-Domain Models

The frequency-domain numerical methods outlined in Section 2.1 are essential for a thorough understanding of the dynamics of wave energy converters (WECs) and their operational principles. However, these techniques rely on linearity within the system. Time-domain models, on the other hand, can handle nonlinearities originating from various stages of the energy conversion process, as well as more intricate formulations for fluid interaction and damping mechanisms, resulting in nonlinear hydrodynamic forces. Moreover, time-domain methods enable the modeling of transient scenarios which could be critical in some cases that cannot be captured in a frequency-domain approach, which is limited to stationary processes.However, time-domain methods are considerably more computationally demanding compared to frequency-domain approaches.

2.2.1 The Cummins Equation for Modelling

Implementing the Cummins equation for the floating body under wave forces F^{WAV} yields:

$$\begin{aligned} &\sum_{j=1}^{6} \left(\left(M_{ij} + A_{ij}^{\infty} \right) \ddot{x}_j(t) + \int_{-\infty}^{t} K_{ij}(t-\tau) \dot{x}_j(\tau) d\tau + C_{ij} x_j(t) \right) \\ &\quad = F_i^{\mathrm{wav}}(t)(x, \dot{x}, t) \end{aligned} \tag{2.33}$$

where M_{ij} and C_{ij} denote elements from the mass matrix and restoring coefficient matrix respectively, A_{ij}^{∞} is the added mass at infinite frequency and $K(t)$ is the radiation impulse response function (RIRF).
From this formulation, it is easy to find that the system is causal and this is ensuring the response of the floating body aligns with the dynamics induced by external forces and moments, an effect derived from the radiation behavior of water waves.

2.2.2 Wave Excitation Force

1. **Wave Loads in Time-Domain Models**
   In models of wave energy conversion, the energy transmitted by propagating ocean waves is incorporated into the system through the action of forces known as wave 'excitation' forces. In the massive majority of cases, only the first-order excitation forces which is typically oscillating with the frequency of the incident waves are significant and included in the model.

2. **Excitation Forces as Superposition of Harmonic Components**
   For regular monochromatic waves, on the 'j' mode the excitation force exerted can be expressed as:

$$F_{ej}(t) = \Gamma(\omega) A \cos(\omega t + \phi(\omega)), \tag{2.34}$$

   where $\Gamma(\omega)$ is the excitation force coefficient and $\phi(\omega)$ is the phase angle. The phase angle denotes the temporal difference between a peak in the wave profile at a reference point—typically the center of the Wave Energy Converter (WEC)—and a peak in the excitation force. The phase angle information is crucial in systems with multiple degrees of freedom due to the phase discrepancies among the excitation forces affecting various degrees of freedom. The most straightforward approach to modeling first-order wave forces in irregular waves is to use the linear superposition of N independent sinusoidal components:

$$F_{ej}(t) = \sum_{i=1}^{N} \Gamma(\omega_i) A_i \cos(\omega_i t + \phi(\omega_i) + \varphi_i) \tag{2.35}$$

3. **Convolution of the Excitation Force**
   The excitation force in the time domain is linked to its frequency-domain counterpart via an inverse Fourier transform. Specifically, the equation presented in Eq. (2.35) represents a discrete version of the inverse Fourier transform applied to the frequency-domain excitation force, achieved by selecting specific frequencies and phases.

The representation of the wave excitation force in the 'j' mode could be given by:

$$F_{ej}(t) = \int_{-\infty}^{+\infty} h_{fj}(\tau)\eta\left(x_0, y_0, t-\tau\right) d\tau, \tag{2.36}$$

where $h_{ij}(t)$ represents the impulse response function (IRF) of the wave excitation force and $\eta(x_0, y_0, t)$ is the wave elevation at the time t.

4. **Nonlinear Wave Forces**
   Accounting for the nonlinear Froude–Krylov force in the incident wave force is crucial when there are significant changes to the wet surface, which may result from the amplitude of the incident wave, the amplitude of the body's movements, or both.

2.2.3 Radiation Impulse Response Function

If we regard the velocity amplitude as an input to the dynamic system, we can treat this unitary radiation force as a frequency-domain transfer function for the radiation force. Thus, the force exerted on degree of freedom 'i' due to motion in degree of freedom 'j' can be written as follows::

$$\hat{F}_{ij}(\omega) = \hat{U}_j \hat{f}_{ij}(\omega) \tag{2.37}$$

where $\hat{f}_{ij}(\omega)$ is the radiation transfer function, defined with added mass and damping coefficient:

$$\begin{aligned} \omega A_{ij} &= \mathrm{Im}\left(-\hat{f}_{ij}\right) \\ B_{ij} &= \mathrm{Re}\left(-\hat{f}_{ij}\right) \end{aligned} \tag{2.38}$$

By applying an inverse Fourier transform to Eq.(2.37), we obtain:

$$F_{kj}(\mathrm{t}) = \int_{-\infty}^{\infty} \widetilde{U}_j(\tau)\widetilde{f}_{kj}(t-\tau)d\tau \tag{2.39}$$

We could rewrite radiation transfer function by knowing Eq.(2.38) as:

$$\hat{f}_{ij}(\omega) = -\mathrm{i}\omega\left(\bar{A}_{ij}(\omega) + A_{ij}^{\infty}\right) - B_{ij}(\omega). \tag{2.40}$$

And accordingly the inverse Fourier transform of the radiation transfer function is:

$$\widetilde{f}_{ij}(t) = \frac{1}{2\pi}\int_{-\infty}^{\infty}\left(-\mathrm{i}\omega\bar{A}_{ij}(\omega) - B_{ij}(\omega)\right)\mathrm{e}^{\mathrm{i}\omega t}d\omega - A_{ij}^{\infty}\dot{\delta}(t) \tag{2.41}$$

and defining

$$K_{ij}(t) = \frac{1}{2\pi}\int_{-\infty}^{\infty}\left(\mathrm{i}\omega\bar{A}_{ij}(\omega) + B_{ij}(\omega)\right)\mathrm{e}^{\mathrm{i}\omega t}d\omega \tag{2.42}$$

By combining these equations together and considering that K_{ij} is real and causal, radiation force could be described by:

$$F_{ij}(t) = -\int_{-\infty}^{t} \tilde{U}_j(\tau) K_{ij}(t-\tau) d\tau - A_{ij}{}^{\infty} \dot{\tilde{U}}_j(\tau) \tag{2.43}$$

Since the RIRF is real, $\hat{K}_{ij}$ could be seen as a Hermitian matrix, whose real part is an even function of ω and imaginary part is odd function of ω. This implies that Eq.(2.42) could be written as:

$$K_{ij}(t) = \frac{1}{\pi} \int_0^{\infty} \left(-\omega \bar{A}_{ij}(\omega) \sin \omega t + B_{ij}(\omega) \cos \omega t \right) d\omega \tag{2.44}$$

Considering that $\hat{K}_{ij}$ is causal which inferred by the fact that it represents the effect of the past body oscillations on its actual state, $\hat{K}_{ij}$ is zero when $t < 0$ and this relation is derived:

$$-\int_0^{\infty} \omega \bar{A}_{ij}(\omega) \sin \omega t d\omega = \int_0^{\infty} B_{ij}(\omega) \cos \omega t d\omega \text{ for } t < 0 \tag{2.45}$$

Using this relation, $\hat{K}_{ij}$ becomes:

$$\begin{aligned} K_{ij}(t) &= \frac{2}{\pi} \int_0^{\infty} B_{ij}(\omega) \cos \omega t d\omega \\ K_{ij}(t) &= -\frac{2}{\pi} \int_0^{\infty} \omega \bar{A}_{ij}(\omega) \sin \omega t d\omega \end{aligned} \tag{2.46}$$

2.3 System Identification

System identification is a method to determine models from input/output data measured from the system.
The identification process follows a series of steps. Initially, a parametric model structure is selected. Subsequently, an appropriate input signal is administered to stimulate the system, and the response is recorded. Utilizing the captured input and output signals, an identification algorithm is employed to ascertain the optimal model parameters. These parameters are determined to minimize the error between the measured output and the output anticipated by the identified parametric model. The concept of model identification from recorded wave energy converter (WEC) data is illustrated below:

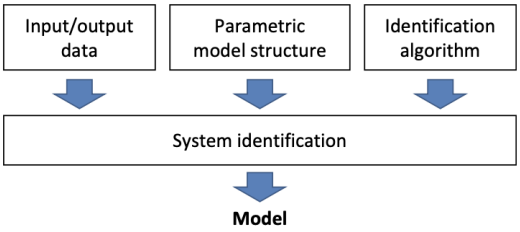

Figure 2.1: System identification procedure

A significant challenge in system identification lies in ensuring that the input/output data utilized to establish the model adequately represents the system dynamics. In the context of wave energy converters, it should encompass a spectrum of frequencies and amplitudes expected during system operation.
A convincing approach to generating appropriate input/output data is by utilizing a Numerical Wave Tank (NWT). An NWT refers to a class of numerical simulators designed to model nonlinear free surface waves, hydrodynamic forces, and floating body motions.
This approach could encompass an enough range of frequencies and amplitude of excitation waves not like using open ocean to collect input data. And this approach is economical compared to a tank test and it also avoids the problems brought from tank wall reflections. But it do have drawbacks like extremely long time to perform the numerical computation of the response and evaluating the accuracy of an NWT simulation proves challenging without experimental validation and may be constrained by numerical diffusion.

2.4 Numerical Solver NLFK4ALL

As discussed in the last section, utilizing numerical wave tank(NWT) which basically is a mathematical model is a promising approach to generate data. Extensive parametric studies are necessary to optimize energy cost-effectiveness, aiming to enhance power extraction capabilities while minimizing capital and operational expenses. Moreover, model-based control strategies, crucial for maximizing WEC performance, demand accurate and real-time mathematical models. So efficient computation is a critical requirement as well as accuracy for mathematical models employed in design processes, especially for wave energy converters. Balancing accuracy and computational efficiency poses a challenge, necessitating a suitable compromise.

In this research, an open-source solver called NLFK4ALL which offering a readily applicable implementation across multiple degrees of freedom is used to collected data. This is an nonlinear Froude-Krylov (NLFK) force model tailored

for axisymmetric floaters. Leveraging the geometry's symmetry, common in WECs, enables achieving rapid computation, approximately in real-time. Furthermore, as nonlinear Froude-Krylov (NLFK) forces constitute primary nonlinearities in such devices, the model attains higher accuracy compared to linear models.

2.4.1 Reference Frame

1. **World and body-fixed frames**
   Two right-handed frames of reference are used:

   - World-frame(WF): $(x, y, z)'$
   - Body-fixed frame(BF): $(\hat{x}, \hat{y}, \hat{z})'$

   The inertial world-frame of reference $(x, y, z)'$ has its origin at the still water level (SWL), with the x-axis extending positively in the direction of wave propagation, and the z-axis extending positively upwards. The body-fixed frame of reference $(\hat{x}, \hat{y}, \hat{z})'$ is non-inertial, with the origin anchored at a reference point (RefP), typically located at the centre of gravity (CoG) or at the SWL, and the z-axis oriented upwards.
   The revolution function of the axisymmetric floater is defined as $f(\varrho)$ between ϱ_1 and ϱ_2 using cylindrical coordinates. So the coordinates points of surface of floater could be written as:

$$\begin{cases} \hat{x}(\varrho, \vartheta) = f(\varrho)\cos\vartheta \\ \hat{y}(\varrho, \vartheta) = f(\varrho)\sin\vartheta \\ \hat{z}(\varrho, \vartheta) = \varrho \end{cases} , \quad \vartheta \in [-\pi, \pi) \wedge \varrho \in [\varrho_1, \varrho_2] \tag{2.47}$$

   And the displacement of the RefP in WF coordinates is denoted by $(x_R, y_R, z_R)'_{\text{WF}}$.

2. **Translation and Rotation**
   By applying 3-2-1 Euler rotation sequence, the rotation matrix which is around the RefP and about the body-fixed axes, *Rot* is defined as:

$$Rot = \begin{bmatrix} c\psi & -s\psi & 0 \\ s\psi & c\psi & 0 \\ 0 & 0 & 1 \end{bmatrix} \begin{bmatrix} c\theta & 0 & s\theta \\ 0 & 1 & 0 \\ -s\theta & 0 & c\theta \end{bmatrix} \begin{bmatrix} 1 & 0 & 0 \\ 0 & c\phi & -s\phi \\ 0 & s\phi & c\phi \end{bmatrix} \tag{2.48}$$

   where ϕ is the roll angle around the $\hat{x}$-axis, θ is the pitch angle around the $\hat{y}$-axis, and ψ is the yaw angle around the $\hat{z}$-axis.
   After the rotation, apply the translation $C = (x_R, y_R, z_R + z_{\text{RefP }P})'_{\text{WF}}$. By

combining rotation and translation, compact matrix R is defined:

$$R = \left(\begin{array}{ccc|c} & Rot & & C \\ \hline 0 & 0 & 0 & 1 \end{array}\right) \tag{2.49}$$

So the transformation from BF to WF is easily given by:

$$\begin{pmatrix} x \\ y \\ z \\ 1 \end{pmatrix} = R \begin{pmatrix} \hat{x} \\ \hat{y} \\ \hat{z} \\ 1 \end{pmatrix} \tag{2.50}$$

3. **Intersection**
In order to represent the instantaneous wet surface of the floater analytically, the analytical definition of the intersection between the body-surface and free surface elevation which is decribed by an arbitrary function the need to be defined.
In general, a typical irregular wave could be written as:

$$\eta(x,t) = \sum_{i=1}^{N_\omega} a_i \cos\left(\omega_i t + \varphi_i - k_i x\right), \tag{2.51}$$

where a_i, ω_i, φ_i, and k_i are the wave amplitudes, frequencies, phases, and wave numbers, respectively.
The wave surface is defined in the WF as:

$$\Gamma = \begin{pmatrix} x \\ y \\ \eta(x) \\ 1 \end{pmatrix} \tag{2.52}$$

So wave surface is defined in the BF is: $\hat{\Gamma} = R^{-1}\Gamma$. The intersection is found by equating ϱ to the third line of $\hat{\Gamma}$ which means:$\varrho = (0,0,1,0)R^{-1}\Gamma$. And by representing Γ as a function of ϱ and θ, rewrite the equation as:

$$\begin{aligned} &f(\varrho)\left(\cos\vartheta\left(R_{11}R_{13} + R_{21}R_{23}\right) + \sin\vartheta\left(R_{12}R_{13} + R_{22}R_{23}\right)\right) + \\ &\varrho\left(R_{13}^2 + R_{23}^2 - 1\right) + R_{33}(\eta(\vartheta,\varrho) - C(3))\Big) = 0 \end{aligned} \tag{2.53}$$

2.4.2 Integration

An integral I of a generic function $g(\hat{x}, \hat{y}, \hat{z})$ over a surface S could be mapped to $g(u, v)$:

$$\begin{aligned} I &= \iint_S g(\hat{x}, \hat{y}, \hat{z}) dS \\ I &= \int_u \int_v g(u, v) \left\| \mathbf{e}_u \times \mathbf{e}_v \right\| du dv \end{aligned} \tag{2.54}$$

where e_u and e_v are the unity vectors in the u and v direction, respectively:

$$\begin{aligned} \mathbf{e}_u &= \begin{pmatrix} \frac{\partial \hat{x}}{\partial u} \\ \frac{\partial \hat{y}}{\partial u} \\ \frac{\partial \hat{z}}{\partial u} \end{pmatrix} \\ \mathbf{e}_v &= \begin{pmatrix} \frac{\partial \hat{x}}{\partial v} \\ \frac{\partial \hat{y}}{\partial v} \\ \frac{\partial \hat{z}}{\partial v} \end{pmatrix} \end{aligned} \tag{2.55}$$

1. **Parametric representations**
   Hereafter cylindrical coordinates are shown, along with the unity and normal unity vector n:

$$\begin{aligned} &\begin{cases} \hat{x}(\varrho, \vartheta) = f(\varrho) \cos \vartheta \\ \hat{y}(\varrho, \vartheta) = f(\varrho) \sin \vartheta \\ \hat{z}(\varrho, \vartheta) = \varrho \end{cases} \quad , \quad \vartheta \in [-\pi, \pi) \wedge \varrho \in [\varrho_1, \varrho_2] \\ &\mathbf{e}_\varrho = \begin{pmatrix} f(\varrho)' \cos \vartheta \\ f(\varrho)' \sin \vartheta \\ 1 \end{pmatrix} \\ &\mathbf{e}_\vartheta = \begin{pmatrix} -f(\varrho) \sin \vartheta \\ f(\varrho) \cos \vartheta \\ 0 \end{pmatrix} \\ &\mathbf{e}_\varrho \times \mathbf{e}_\vartheta = f(\varrho) \begin{pmatrix} -\cos \vartheta \\ -\sin \vartheta \\ f(\varrho)' \end{pmatrix} \\ &\left\| \mathbf{e}_\varrho \times \mathbf{e}_\vartheta \right\| = f(\varrho) \sqrt{1 + f(\varrho)'^2} \end{aligned} \tag{2.56}$$

   So the unity normal vector $\mathbf{n}$ over surface is computed as:

$$\iint_S \mathbf{n} dS = \iint_S \frac{\mathbf{e}_\varrho \times \mathbf{e}_\vartheta}{\left\| \mathbf{e}_\varrho \times \mathbf{e}_\vartheta \right\|} dS = \int_\vartheta \int_\varrho (\mathbf{e}_\varrho \times \mathbf{e}_\vartheta) d\varrho d\vartheta \tag{2.57}$$

2. **Normalization of the integration domain**
   The domain of integration for cylindrical coordinates is defined as $\vartheta \in [-\pi, \pi) \wedge$

$\varrho \in [\varrho_1, \varrho_2]$ and it is convenient to map it to $\vartheta \in [-\pi, \pi) \wedge \tilde{\varrho} \in [0,1]$ where $\tilde{\varrho} = \varrho_1 + \varrho\,(\varrho_2(\vartheta) - \varrho_1)$. So the unity normal vector $\mathbf{n}$ over surface could be rewritten as:

$$\begin{aligned} \iint_S \mathbf{n} dS &= \int_{-\pi}^{\pi} \int_{\varrho_1}^{\varrho_2} \left(\mathbf{e}_\varrho(\varrho, \vartheta) \times \mathbf{e}_\vartheta(\varrho, \vartheta)\right) d\varrho d\vartheta \\ &= \int_{-\pi}^{\pi} \int_{0}^{1} \left(\mathbf{e}_\varrho(\tilde{\varrho}, \vartheta) \times \mathbf{e}_\vartheta(\tilde{\varrho}, \vartheta)\right) (\varrho_2(\vartheta) - \varrho_1)\, d\tilde{\varrho} d\vartheta \end{aligned} \tag{2.58}$$

3. **Geometric Properties**

   - **Surfaces**
     The total surface S is composed of the lateral surface S_L plus the bottom S_{bot} and top S_{top} discs.

$$\begin{aligned} S_{bot} &= \iint_{S_{bot}} dS = \int_\vartheta \int_r \|\mathbf{e}_\vartheta \times \mathbf{e}_r\|\, d\vartheta dr = \int_{2\pi}^{\pi} \int_0^{R_1} r d\vartheta dr = \pi R_1^2 \\ S_L &= \iint_{S_L} dS = \int_\vartheta \int_\varrho \|\mathbf{e}_\vartheta \times \mathbf{e}_\varrho\|\, d\vartheta d\varrho = \int_\vartheta \int_\varrho f(\varrho)\sqrt{1 + f(\varrho)^2} d\vartheta d\varrho \end{aligned} \tag{2.59}$$

   - **Volumn**

$$V = -\iint_S n_1 \hat{x} dS = -\iint_S n_2 \hat{y} dS = -\iint_S n_3 \hat{z} dS \tag{2.60}$$

   - **Centre of buoyancy**
     The centre of buoyancy $CoB = (\hat{x}_B, \hat{y}_B, \hat{z}_B)$ is the centroid of the displaced volume of fluid by the floater. Considering that the body is axisymmetric, $\hat{x}_B$ and $\hat{y}_B$ are null. The resulting integral for $\hat{z}_B$ is:

$$\hat{z}_B = -\frac{1}{2V}\left(\int_{-\pi}^{\pi} \int_{\varrho_1}^{\varrho_0} \varrho^2 f(\varrho) f(\varrho)' d\varrho d\vartheta + \pi R_1^2 \varrho_1^2 - \pi R_2^2 \varrho_0^2\right) \tag{2.61}$$

     where ϱ_0 as the body-frame vertical coordinate of the still water level.

2.4.3 Nonlinear Froude-Krylov force

The Froude-Krylov force originates from the pressure distribution on the surface of the WEC induced by incident waves. In the world-frame, the pressure field p follows Airy's theory and incorporates Wheeler stretching, represented as:

$$p(x, z, t) = p_{st} + p_{dy} = -\rho g z + \rho g a \cos(\omega t - kx) \frac{\cosh\left(k\left(z' + h\right)\right)}{\cosh(kh)} \tag{2.62}$$

where p_{st} and p_{dy} are the static and dynamic pressure, a is the wave amplitude, $\omega = \frac{2\pi}{T}$ is the wave frequency and T the wave period, $k = \frac{2\pi}{\lambda}$ is the wave number and

λ the wave length, h is the water depth. Specially, z' is the change of coordinates in order to eliminate the free surface boundary condition error: $z' = h\frac{z+h}{\bar{\eta}+h} - h$, where $\bar{\eta}$ is an approximation of the free surface.

The static and dynamic Froude-Krylov force is then defined as:

$$\begin{aligned} \mathbf{F}_{FK_{dy}} &= \iint_{S_w} p_{dy}\mathbf{n}dS \\ \mathbf{F}_{FK_{dy}} &= \iint_{S_w} p_{dy}\mathbf{n}dS \end{aligned} \tag{2.63}$$

where $\mathbf{F}_g = (0,0,-mg)'$ is the gravity force, with m the mass of the body, S_w the instantaneous wet surface, and n the unity vector normal to the surface. Accordingly, static and dynamic Froude-Krylov torques are defined as:

$$\begin{aligned} \mathbf{T}_{FK_{st}} &= \mathbf{r}_g \times \mathbf{F}_g + \iint_{S_w} p_{st}(\mathbf{r} \times \mathbf{n})dS \\ \mathbf{T}_{FK_{dy}} &= \iint_{S_w} p_{dy}(\mathbf{r} \times \mathbf{n})dS \end{aligned} \tag{2.64}$$

where r is the generic position vector, and r_g is the position vector of the centre of gravity.
It is easier to write the equation of motion in the body-fixed frame where inertial matrix is constant and the NLFK forces are computed in the BF too. But the free surface elevation and the pressure field are defined in world-frame. Therefore, η and p could be mapped into the BF and compute the integrals directly in the BF by 4D rotaion matrix $\mathbf{R}$. And hereafter are $\mathbf{n}dS$ and $(\mathbf{r} \times \mathbf{n})dS$, after the change or coordinate transformation, in polar and cylindrical coordinates:

$$\begin{aligned} \mathbf{r} &= \begin{cases} \hat{x}(\varrho,\vartheta) = f(\varrho)\cos\vartheta \\ \hat{y}(\varrho,\vartheta) = f(\varrho)\sin\vartheta \\ \hat{z}(\varrho,\vartheta) = \varrho \end{cases}, \quad \vartheta \in [-\pi,\pi) \wedge \varrho \in [\varrho_1,\varrho_2] \\ \mathbf{n}dS = \mathbf{e}_\varrho \times \mathbf{e}_\vartheta &= f(\varrho)\begin{pmatrix} -\cos\vartheta \\ -\sin\vartheta \\ f(\varrho)' \end{pmatrix} \\ (\mathbf{r} \times \mathbf{n})dS = \mathbf{r} \times (\mathbf{e}_\varrho \times \mathbf{e}_\vartheta) &= \begin{pmatrix} f(\varrho)\sin\vartheta\,(f(\varrho)f(\varrho)' + \varrho) \\ -f(\varrho)\cos\vartheta\,(f(\varrho)f(\varrho)' + \varrho) \\ 0 \end{pmatrix} \end{aligned} \tag{2.65}$$

2.5 Excitation Waves

In numerical wave tank simulations, the accurate representation of wave excitation is essential for modeling the dynamic behavior of wave energy converters (WECs)

and simulating real-world wave conditions. Two primary types of excitation waves are utilized in these simulations: multinse waves for model building and waves to simulate real ocean states.

2.5.1 Irregular Waves to Simulate Real Ocean

Real ocean could be modeled as the linear superposition of a large number of harmonic waves at different frequencies and angles of incidence, where the incident wave is defined as $\eta(x, y, t)$:

$$\eta(x, y, t) = \sum_i \frac{H_i}{2} \cos\left(\omega_i t - k_i \left(x \cos\theta_i + y \sin\theta_i\right) + \phi_i\right) \tag{2.66}$$

where H is the wave height, ω is the wave frequency $\left(\omega = \frac{2\pi}{T}\right), k$ is the wave number $\left(k = \frac{2\pi}{\lambda}\right), \theta$ is the wave direction, and ϕ is the wave phase (randomized for irregular waves).
The frequency domain representation of linearly superimposed regular waves with varying amplitudes and periods is defined by a wave spectrum. These spectra are defined by certain parameters including significant wave height, peak period, wind speed, fetch length, and etc, which are determined through statistical analysis.

- **Pierson–Moskowitz (PM) Spectrum**
  The Pierson-Moskowitz (PM) spectrum is used for a fully developed sea, where wave growth is unrestricted by fetch. It's a two-parameter spectrum determined by significant wave height and peak wave frequency. By adjusting the peak frequency for a given significant wave height, various sea conditions from developing to decaying seas can be accounted for. These parameters are mainly influenced by wind speed, wind direction, fetch, and storm front locations. PM spectrum[17] is defined by:

$$\begin{aligned} S_{PM}(f) &= \frac{{H_{m0}}^2}{4} \left(1.057 f_p\right)^4 f^{-5} \exp\left[-\frac{5}{4}\left(\frac{f_p}{f}\right)^4\right] \\ A_{ws} &= \frac{{H_{m0}}^2}{4} \left(1.057 f_p\right)^4 \approx \frac{5}{16} {H_{m0}}^2 {f_p}^4 \approx \frac{B_{ws}}{4} {H_{m0}}^2 \\ B_{ws} &= \left(1.057 f_p\right)^4 \approx \frac{5}{4} {f_p}^4 \end{aligned} \tag{2.67}$$

- **JONSWAP (JS) Spectrum** The JONSWAP (Joint North Sea Wave Project) spectrum is an adaptation of the PM spectrum designed for developing sea states within a fetch-limited environment. It incorporates a higher peak and

a narrower spectrum during stormy conditions, while maintaining the same total energy as the PM spectrum. JS spectrum[17] is defined by:

$$
\begin{aligned}
&S_{JS}(f) = C_{ws}(\gamma) S_{PM} \gamma^{\alpha} \\
&C_{ws}(\gamma) = \frac{\int_0^{\infty} S_{PM}(f) df}{\int_0^{\infty} S_{PM}(f) \gamma^{\alpha} df} = 1 - 0.287 \ln(\gamma) \\
&\alpha = \exp\left[-\left(\frac{\frac{f}{f_p} - 1}{\sqrt{2}\sigma} \right)^2 \right], \sigma = \begin{cases} 0.07 & f \leq f_p \\ 0.09 & f > f_p \end{cases} \\
&\gamma = \begin{cases} 5 & \text{for } \frac{T_p}{\sqrt{H_{m0}}} \leq 3.6 \\ \exp\left(5.75 - 1.15 \frac{T_p}{\sqrt{H_{m0}}}\right) & \text{for } 3.6 \leq \frac{T_p}{\sqrt{H_{m0}}} \leq 5 \\ 1 & \text{for } \frac{T_p}{\sqrt{H_{m0}}} > 5 \end{cases}
\end{aligned}
\tag{2.68}
$$

2.5.2 Multisine Waves for Model Building

Multisine waves serve as useful tools for model development and validation within numerical wave tank simulations. These waves are generated using spectral methods, which synthesize wave spectra corresponding to different sea states and wave climates. The fundamental principle behind spectral wave generation is the superposition of individual wave components, each characterized by its amplitude, frequency, and phase. Mathematically, the surface elevation $\eta(t)$ of a multisine wave can be represented as:

$$
\eta(t) = \sum_{i=1}^{N} A_i \cos\left(\omega_i t + \phi_i\right) \tag{2.69}
$$

where:
- A_i is the amplitude of the i th wave component,
- ω_i is the angular frequency,
- ϕ_i is the phase angle, and
- N is the total number of wave components.

By synthesizing multinse waves with varying characteristics, researchers can explore the dynamic response of WECs under different wave conditions, facilitating model validation and performance assessment.

Moreover, phases are often adjusted or optimized to minimize the crest factor (peak to RMS ratio) and thereby enhance the signal-to-noise ratio (SNR) for frequency response function (FRF) measurements. This optimization is necessary because physical systems typically have limited maximum excitation amplitudes. One common choice for optimizing phases is the use of Schröder phases[18]:

$$
\phi_k = \frac{-k(k-1)\pi}{N_k} \tag{2.70}
$$

Chapter 3

Implementing two DoF

3.1 Hydrodynamic WEC modelling

In this section, we recall foundational principles underpinning the intricate nonlinear hydrodynamic modeling, particularly tailored for the dynamic interplay within wave energy conversion systems. The modelling is firmly rooted in the potential flow theory, a basic approach in fluid dynamics that offers profound insights into the behavior of fluid-solid interactions, together with the frequency-domain model and time-domain model describe in Chapter 2. Driven by a pursuit of clarity, we make a deliberate choice to narrow our focus to devices within two degrees of freedom (DoF) which is heave and pitch. By simplifying our exposition to two degrees of freedom framework, we aim to enhance the accessibility of our discourse while preserving the essence of the underlying principles.

Recalling the second law of Newton as describe in Eq.(2.17), the force acting on the floater could be decomposed to two parts, gravity and forces exerted by water:

$$\begin{aligned} m_z\ddot{z}(t) &= m_z g - F_z \\ m_p\ddot{p}(t) &= m_p g - F_p \end{aligned} \tag{3.1}$$

where m_z is the mass of the floater and m_p is the moment of inertia of y-axis. According to flow theory $\phi(t) = \phi_{\mathrm{I}} + \phi_{\mathrm{d}} + \phi_{\mathrm{r}}$ (ϕ_{I} is incident wave, $\phi_{\mathrm{d}}$is diffraction wave and $\phi_{\mathrm{r}}$is radiation wave as described in Eq.(2.13), forces exerted by water could be decomposed as:

- $\mathbf{F}_{FK}^{dyn}$ is the dynamic Froude-Krylov force:

$$\mathbf{F}_{FK}^{dyn}(t) = -\iint_{S(t)} P_{dy}(t)\mathbf{n}\mathrm{d}S \tag{3.2}$$

  where $P_{dy} = -\rho\frac{\partial\phi_I}{\partial t} - \rho\frac{|\nabla\phi_I|^2}{2}$ the dynamic pressure.

- $\mathbf{F}_d$ is the diffraction force:

$$\mathbf{F}_d(t) = -\iint_{S(t)} P_d(t)\mathbf{n}\mathrm{d}S \tag{3.3}$$

where $P_d = -\rho\frac{\partial\phi_d}{\partial t} - \rho\frac{|\nabla\phi_d|^2}{2}$ the diffraction pressure. And it could be also described as:

$$\mathbf{F}_d(t) = k_\mathrm{d} * \eta \tag{3.4}$$

where the impulse response $k_\mathrm{d} : \mathbb{R}^+ \to \mathbb{R}, k_\mathrm{d} \in L^2(\mathbb{R})$, fully characterises a linear time-invariant system with input η and output $\mathbf{F}_d(t)$.

Remark the diffraction kernel k_d is always calculated numerically using Boundary Element Method (BEM) solvers in a non-parametric form.

- $\mathbf{F}_R$ is the radiation force:

$$\mathbf{F}_R(t) = -\iint_{S(t)} P_R(t)\mathbf{n}\mathrm{d}S \tag{3.5}$$

where $P_R = -\rho\frac{\partial\phi_R}{\partial t} - \rho\frac{|\nabla\phi_R|^2}{2}$ the radiation pressure. This radiation force could be modelled as the time-domain model specially proposed in Section 2.23, write radiation forced constraited to heave and pitch mode:

$$F_{\mathrm{rad}}\,(t) = -A_\infty\ddot{\xi} - \int_0^t K_r(t-\tau)\dot{\xi}(\tau)d\tau \tag{3.6}$$

where $\xi = (z, p)$ is generalized floater displacement. So it can be also written in convolution form:

$$\mathbf{F}_\mathrm{R}(t) = -A_\infty\ddot{\xi} - k_\mathrm{r} * \dot{\xi} \tag{3.7}$$

Remark Transforming the radiation convolution integral into state-space (SS) representation is greatly advantageous. Such a transformation has been demonstrated to significantly enhance computational efficiency, enabling the application of conventional control techniques reliant on linear state-space models.

- Since the fluid is assumed to be inviscid, there is also viscous force and it is modelled using the Morrison equation:

$$\mathbf{F}_{vis} = -\frac{1}{2}\rho C_d A_d\,|\mathbf{V} - \mathbf{V_0}|\,(\mathbf{V} - \mathbf{V_0}) \tag{3.8}$$

where C_d is the drag coefficient, A_d is the characteristic surface, V is the velocity of the floater and V_0 is the undisturbed flow velocity.

- Static Froude-Krylov force is an exception because it is not just stemming from waves, instead it is given as the balance between the gravity force and the Archimedes force:

$$\mathbf{F}_{FK_{st}}(t) = \mathbf{F}_g - \iint_{S(t)} P_{st}(t)\mathbf{n}\mathrm{d}S \tag{3.9}$$

  where $P_{\mathrm{st}} = -\rho g z$.

Define $z : \mathbb{R}^+ \to \mathbb{R}, t \mapsto z(t)$ as device displacement in heave mode, $p : \mathbb{R}^+ \to \mathbb{R}, t \mapsto p(t)$ as device displacement in pitch mode and $\eta : \mathbb{R}^+ \to \mathbb{R}$, $t \mapsto \eta(t)$ be undisturbed free-surface elevation which is measured at the centre of the body's reference frame. The dynamic behavior of such a Wave Energy Converter (WEC) system can be formulated within a system Σ_{W}, applicable for $t \in \mathbb{R}^+$, as follows:

$$\Sigma_{\mathrm{W}} : \begin{cases} \mathbf{M}\ddot{\xi} = f_{\mathrm{r}}(\xi) + f_{\mathrm{v}}(\dot{\xi}) + f_{\mathrm{d}}(\eta) + \\ \qquad f_{\mathrm{FK}}^{\mathrm{st}}(\eta, \xi) + f_{\mathrm{FK}}^{\mathrm{dyn}}(\eta, \xi), \\ y = C \begin{bmatrix} \xi & \dot{\xi} \end{bmatrix}^\top, \end{cases} \tag{3.10}$$

where $\mathbf{M}$ is a matrix of mass and moment of inertia in y-axis and it is written as: $\begin{bmatrix} m & 0 \\ 0 & I_{yy} \end{bmatrix}$. $f_{\mathrm{r}} : \mathbb{R}^2 \to \mathbb{R}^2$ is the radiation force and it could be written as $f_{\mathrm{r}}(\dot{\xi}) = -A_\infty \ddot{\xi} - k_{\mathrm{r}} * \dot{\xi}$. $f_{\mathrm{v}} : \mathbb{R}^2 \to \mathbb{R}^2$ is the viscous effects, $f_{\mathrm{d}} : \mathbb{R} \to \mathbb{R}^2$ reprensents the diffraction force, and the mappings $f_{\mathrm{FK}}^{\mathrm{st}} : \mathbb{R} \times \mathbb{R}^2 \to \mathbb{R}^2$ represents the static Froude-Krylov (FK) effects (or forces) and $f_{\mathrm{FK}}^{\mathrm{dyn}} : \mathbb{R} \times \mathbb{R}^2 \to \mathbb{R}^2$, represent the dynamic Froude-Krylov (FK) effects (or forces) instead. The output $y : \mathbb{R}^4 \to \mathbb{R}^2$ is considered to be a linear combination of device velocity and displacement, defined by the matrix $C^\top \in \mathbb{R}^{2\times 4}$.

3.2 Generating data

3.3 Modelling Static FK effect

The mapping function f_{FK}^{st} represents a static function that relies on the free-surface elevation η and the heave of the device z and pitch of the device p. While analytical derivations for f_{FK}^{st} exist for certain geometries like a purely pitching prismatic device[13], the aim of this section is to introduce a comprehensive data-driven approach. This methodology is designed to be universally applicable, irrespective of the particular shape of the device, ensuring versatility across various device configurations and geometries.
This mapping function could be seen from a system-theoretic perspective and

expressed as Σ^{st}, where the input of this system is heave displacement z, pitch displacement p, free-surface elevation η and the output is the static Froude-Krylov force in term of heave and pitch.

$$\Sigma^{\mathrm{st}} : \begin{cases} y^{\mathrm{st}} = \begin{bmatrix} y^{\mathrm{st_z}} \\ y^{\mathrm{st_p}} \end{bmatrix} = f_{\mathrm{FK}}^{\mathrm{st}}(\eta, z, p) \end{cases} \tag{3.11}$$

The following assumption have to be made to develop a data-based approximation towards static Froude-Krylov force. It assumes that the mapping $f_{\mathrm{FK}}^{\mathrm{st}}$ belongs to the function space identified by the family of continuous basis functions $\phi_j : \mathbb{R}^3 \to \mathbb{R}$, with $j = 1, \ldots, M$ (where M may be ∞). In other words, there exist constants $a_j^z \in \mathbb{R}$ and $a_j^p \in \mathbb{R}$, with $j = 1, \ldots, M$, such that

$$f_{\mathrm{FK}}^{\mathrm{st}}(\eta, z, p) = \begin{bmatrix} \sum_{j=1}^{M} a_j^z \phi_j(\eta, z, p) \\ \sum_{j=1}^{M} a_j^p \phi_j(\eta, z, p) \end{bmatrix}, \tag{3.12}$$

for any η, z, and p. And intuitively when there is no incident wave, the floater will be still: $\phi_j(0,0,0) = 0$.
The standard assumption that the mapping to be approximated can be expressed using a family of basis functions is commonplace. In practice, a trial-and-error approach can be adopted. For example, one might begin by employing a polynomial expansion or an expansion based on functions akin to those generated by the signal generator like sinusoids for sinusoidal inputs.
Thus, let

$$\begin{aligned} \mathcal{P} &= \begin{bmatrix} a_1^z & a_2^z & \cdots & a_N^z \\ a_1^p & a_2^p & \cdots & a_N^p \end{bmatrix} \\ \Phi(\eta, z, p) &= \begin{bmatrix} \phi_1(\eta, z, p) & \phi_2(\eta, z, p) & \ldots & \phi_N(\eta, z, p) \end{bmatrix}^\top \end{aligned} \tag{3.13}$$

with $N \leq M$. Using a weighted sum of basis functions, Eq. (3.2) can be written as

$$f_{\mathrm{FK}}^{\mathrm{st}}(\eta, z, p) = \begin{bmatrix} \sum_{j=1}^{N} a_j^z \phi_j(\eta, z, p) + e^z(\eta, z, p) \\ \sum_{j=1}^{N} a_j^p \phi_j(\eta, z, p) + e^p(\eta, z, p) \end{bmatrix} \tag{3.14}$$

where $e(t) = \sum_{N+1}^{M} a_j \phi_j(\eta, z, p)$ is the error resulting by terminating the summation at N. So now consider the approximation

$$\tilde{f}_{\mathrm{FK}}^{\mathrm{st}}(\eta, z, p) = \begin{bmatrix} \sum_{j=1}^{N} a_j^z \phi_j(\eta, z, p) \\ \sum_{j=1}^{N} a_j^p \phi_j(\eta, z, p) \end{bmatrix} = \mathcal{P}\Phi(\eta, z, p) \tag{3.15}$$

which neglects the truncating error $e(t)$.
So the approximating system could be represented as:

$$\tilde{\Sigma}^{\mathrm{st}} : \begin{cases} \tilde{y}^{\mathrm{st}} = \tilde{f}_{\mathrm{FK}}^{\mathrm{st}}(\eta, z, p), \end{cases} \tag{3.16}$$

With Equation (3.5), the approximation task boils down to identifying an appropriate matrix $\mathcal{P}$ for any given basis-function vector $\Phi(\eta, z, p)$. Here, we introduce a method to compute $\mathcal{P}$ based on a recursive least-squares approach. Consider $\mathcal{T}_k^w = \{t_{k-w-1}, \ldots, t_{k-1}, t_k\} \subset \mathbb{R}^+$, a set of time instants where we numerically assess the output of the target static FK system, denoted as y^{st} in Equation (3.1). This set essentially represents a moving window of $w \in \mathbb{N}$ samples. Assuming the numerical evaluation of y^{st}, we choose the free-surface elevation η as the external input, typically generated as a multisine signal.(The reason behind of choosing multisine is that it is persistently exciting and set $\mathcal{T}_k^w$ can always be selected such that the above assumption holds without lost of generality) Let $\Xi_k \in \mathbb{R}^{w \times N}$ and $\Upsilon_k \in \mathbb{R}^w$ be defined as:

$$\begin{aligned} \Xi_k &= \begin{bmatrix} \Phi_{t_{k-w-1}} & \ldots & \Phi_{t_{k-1}} & \Phi_{t_k} \end{bmatrix}^\top, \\ \Upsilon_k &= \begin{bmatrix} y^{\text{st}}_{t_{k-w-1}} & \ldots & y^{\text{st}}_{t_{k-1}} & y^{\text{st}}_{t_k} \end{bmatrix}^\top. \end{aligned} \tag{3.17}$$

with $\Phi_{t_r} = \Phi\left(\eta\left(t_r\right), z\left(t_r\right), p\left(t_r\right)\right) \in \mathbb{R}^N$ and $y^{\text{st}}_{t_r} = y^{\text{st}}\ \left(t_r\right) \in \mathbb{R}^2$.

Let $\mathcal{P}_k$ be an on-line estimate of the matrix $\mathcal{P}$ in time window $\mathcal{T}_k^w$, namely computed at the time t_k using the last w instants of time. If Ξ_k is full column rank, then

$$\operatorname{vec}\left(\mathcal{P}_k\right) = \left(\Xi_k^\top \Xi_k\right)^{-1} \Xi_k^\top \Upsilon_k,$$

is an approximation of the estimate $\mathcal{P}_k$.
To ensure that the approximation is well-defined for all k, we need that the elements of T_k^w be selected such that $\Xi_k^\top \Xi_k$ is full column rank aiming to guarantee the upcoming methodology to be well-posed.
The cost function is to determine the quality of $\mathcal{P}_k$ based upon the following criterion:

$$\min_{\mathcal{P}_k} \left\| \Xi_k \mathcal{P}_k^\top - \Upsilon_k \right\|_2^2 \tag{3.18}$$

Now Algorithm 1 is proposed, a recursive method to based on the cost function Eq.(3.8) solve for $\mathcal{P}_k$.

Algorithm 1 unfolds as follows with a more detailed exposition. Initially, meticulous consideration is given to the selection of an optimal multisine signal f_{id} for the generation of the input η. Simultaneously, a carefully chosen initial value k^0, sufficiently large to accommodate the iterative process, is established. The iterative construction of matrices Ξ_k and Υ_k ensues, a step-by-step process reliant on the continuous interplay between the supplied input $\eta = f_{\text{id}}$, the numerically derived device heave motion z and device pitch motion p, and the resultant total static force y^{st}. It's crucial to underscore that the computation of these latter three variables can be conveniently facilitated by utilizing any state-of-the-art

numerical nonlinear FK solver, such as the NLFK4ALL toolbox. And to initialize the recursion process, the selection of P_0 is necessary but it can be accomplished by employing 'dummy' values, which may consist of random values drawn from a uniform distribution. This initial choice serves as a provisional starting point for the recursive algorithm. It's noteworthy that as the algorithm iterates, older measurements become progressively supplanted by newer ones.

At each iteration, when a new set of samples becomes available, the old information is discarded, and the algorithm continues until reaching a certain threshold condition on the error between iterations. This threshold condition is specified by the sufficiently small value ϵ. This iterative process ensures that the algorithm refines its estimates over successive iterations until it converges to an acceptable solution.

Algorithm 1 Static FK approximation. Let k^0 be a sufficiently large integer, and let ϵ be a sufficiently small user-defined error tolerance. Define $\mathcal{P}^0 \in \mathbb{R}^{2\times N}$ as the initialisation vector for the computation of $\mathcal{P}$.

procedure STATIC FK APPROXIMATION(η, z, p)
  ▷ Intitial Conditions:
  ▷ $k = k^0$
  ▷ $\mathcal{E} = \epsilon + 1$
  ▷ $\mathcal{P}_{k-1} = \mathcal{P}^0$
  ▷ Execution
  while $\mathcal{E} > \epsilon$ **do**
    $\Psi_k = \left(\Xi_k^\top \Xi_k\right)^{-1}$
    $\mathcal{P}_k^\top = \mathcal{P}_{k-1}^\top + \Psi_k \Phi_{t_k} \left(y_{t_k}^{\mathrm{st}} - \Phi_{t_k}^\top \mathcal{P}_{k-1}^\top\right) \quad - \Psi_k \Phi_{t_{k-w}} \left(y_{t_{k-w}}^{\mathrm{st}} - \Phi_{t_{k-w}}^\top \mathcal{P}_{k-1}^\top\right)$
    $\mathcal{E} = \left\|\mathcal{P}_k - \mathcal{P}_{k-1}\right\|_2$
    $k = k + 1$
  end while
end procedure

3.4 Modelling Dynamic FK effect

The Dynamic Froude-Krylov (FK) effect refers to the dynamic hydrodynamic forces experienced by a floating or submerged body in response to the motion induced by ocean waves. Unlike the static FK effect, which accounts for the steady-state hydrodynamic forces when the body is stationary, the dynamic FK effect captures the time-varying forces acting on the body as it moves in response to wave motion. This dynamic characteristic invites a system-theoretic interpretation, where f_{FK}^{dyn} can be viewed as the output mapping y^{dyn} originating from a dynamic system Σ^{dyn}.

Like static Froude-Krylov effect, the dynamic one should be decomposed in terms of heave mode and pitch mode:

$$y^{\mathrm{dyn}} = \begin{bmatrix} y^{\mathrm{dyn_z}} \\ y^{\mathrm{dyn_p}} \end{bmatrix} \tag{3.19}$$

Within this system-theoretic framework, free-surface elevation η, heave motion z serve and pitch motion p as inputs, contributing to the dynamical evolution of the system's output representation. This dynamic representation encapsulates the intricate interplay between wave-induced motions and resulting hydrodynamic forces, offering a comprehensive understanding of the dynamic behavior underlying Froude-Krylov forces. And it can be represented as:

$$\Sigma^{\mathrm{dyn}} : \begin{cases} \dot{q} = \kappa(q, \eta, z, p), \\ f_{\mathrm{FK}}^{\mathrm{dyn}} = \theta(q, \eta, z, p) = y^{\mathrm{dyn}} \end{cases} \tag{3.20}$$

where $q(t) \in \mathbb{R}^n$ is the associated state-vector, with $n \in \mathbb{N}$ large enough. The dimensions of mappings is: $\kappa : \mathbb{R}^n \times \mathbb{R} \times \mathbb{R} \times \mathbb{R} \to \mathbb{R}^n$ and $\theta : \mathbb{R}^n \times \mathbb{R} \times \mathbb{R} \times \mathbb{R} \to \mathbb{R}^2$. Due to the physical limitations, the following boundary conditions should be imposed:

- $\kappa(0,0,0,0) = 0$ and $\theta(0,0,0,0) = 0$.
- The zero-equilibrium of system $\dot{q} = \kappa(q, 0,0,0)$ is stable under small perturbations in the vicinity of this point. (Specifically, it means that if the system is initially close to this equilibrium point, its behavior will converge back towards this point over time, and this convergence will occur exponentially fast.)
- For every (q, η, z, p) defined within a extremely small neighborhood $\mathcal{N}$ of $(q, \eta, z, p) = (0, 0, 0, 0)$, the system's behavior can be effectively described by a strictly proper linear system $\tilde{\Sigma}^{\mathrm{dyn}}$. This system has η as its sole external input. To be exact, the following conditions

$$\begin{aligned} \left.\frac{\partial \kappa}{\partial q}\right|_{(0,0,0)} &= F, \left.\frac{\partial \kappa}{\partial \eta}\right|_{(0,0,0)} = G, \left.\frac{\partial \kappa}{\partial z}\right|_{(0,0,0)} = 0, \left.\frac{\partial \kappa}{\partial p}\right|_{(0,0,0)} = 0 \\ \left.\frac{\partial \theta}{\partial q}\right|_{(0,0,0)} &= H, \left.\frac{\partial \theta}{\partial \eta}\right|_{(0,0,0)} = 0, \left.\frac{\partial \theta}{\partial z}\right|_{(0,0,0)} = 0, \left.\frac{\partial \theta}{\partial p}\right|_{(0,0,0)} = 0 \end{aligned}$$

  hold, with $F \in \mathbb{R}^{n \times n}, \{G\} \subset \mathbb{R}^n, \{H\} \subset \mathbb{R}^{2 \times n}$, and therefore system $\tilde{\Sigma}^{\mathrm{dyn}}$ can be written as

$$\tilde{\Sigma}^{\mathrm{dyn}} : \begin{cases} \dot{q}(t) = Fq(t) + G\eta(t), \\ \tilde{f}_{\mathrm{FK}}^{\mathrm{dyn}}(t) = Hq\,(t + t_c) = \tilde{y}^{\mathrm{dyn}}(t), \end{cases} \tag{3.21}$$

where $t_c \in \mathbb{R}^+$, and $\lambda(F) \subset \mathbb{C}_{<0}$ by the second condition above. t_c is necessary because it represents a non-causal time-shift or advance, originates from the scenario where the generated wave, characterized by the free-surface elevation, could potentially influence the WEC body and exert a wave force before any wave has physically reached the central point of the device. This phenomenon underscores the importance of considering the time delay between the initiation of the wave and its interaction with the WEC structure, particularly in modeling dynamic wave forces and their effects on the system dynamics.

Considering that the linear model Eq.(3.11) offers computational simplicity, adheres to the principle of superposition, and facilitates the application of a wide range of mathematical tools for analysis, simulation, and control/estimator design, there is a strong incentive to utilize it. However, existing literature predominantly characterizes the system $\tilde{\Sigma}^{dyn}$ using boundary element method (BEM) solvers like the open-source software Nemoh. These solvers compute the impulse response associated with the system in a non-parametric manner, assuming infinitesimally small device motion around the zero-equilibrium.

Given that the primary design goal for WECs is to maximize energy conversion, which often involves significant induced device motion, this approach is likely to yield an inaccurate linear model for the dynamic Froude-Krylov effect. In contrast to BEM solvers, we propose a methodology to compute a representative linear model $\tilde{\Sigma}^{dyn}$ tailored to specific wave operating conditions of the device, such as significant wave heights and peak periods. To achieve this, we leverage techniques from system identification and introduce a framework for generating representative models using only input-output data in the frequency-domain.

Let $U = \{\eta_i = f_{\mathrm{id}_i}\}_{i=1}^{Q}$ be a set of suitably selected multisine input signals that is free-surface elevation, where $Q \in \mathbb{N}$, generating a corresponding set of outputs $Y = \left\{y_i^{\mathrm{dyn}}\right\}_{i=1}^{Q}$ that is dynamic Froude-Krylov forces. For the system, an input-output pair of signals is represented by $(\eta_i, y_i^{\mathrm{dyn}})$. The empirical transfer function estimate (ETFE), denoted as $H_i : \mathbb{C}^0 \to \mathbb{C}$ and defined by $j\omega \mapsto H_i(j\omega)$, is formulated for each input-output pair using the expression:

$$\begin{aligned} H_i^z(j\omega) &= \frac{\mathcal{Y}_i^{\mathrm{dyn_z}}(j\omega)}{\mathcal{U}_i(j\omega)} \\ H_i^p(j\omega) &= \frac{\mathcal{Y}_i^{\mathrm{dyn_p}}(j\omega)}{\mathcal{U}_i(j\omega)} \end{aligned} \tag{3.22}$$

with $i \in \mathbb{N}$, and where $\mathcal{U}_i : \mathbb{C}^0 \to \mathbb{C}$ and $\mathcal{Y}_i^{\mathrm{dyn}} : \mathbb{C}^0 \to \mathbb{C}$ denote the Fourier

transform of η_i and y_i^{dyn} respectively.
By utilizing the ensemble of ETFE mappings $\mathscr{H} = \{H_i\}_{i=1}^{Q}$, we can efficiently derive the collective ETFE, denoted as $\bar{H}$, which serves the purpose of constructing a more robust and stable input dataset for the frequency-domain identification technique. This aggregated ETFE, computed through a synthesis of individual mappings, aims to minimize variance and enhance reliability, ensuring a more effective utilization within the frequency-domain identification framework. And the average EFET is computed as:

$$\begin{aligned} \bar{H}^z(j\omega) &= \frac{1}{Q}\sum_{i=1}^{Q} H_i^z(j\omega) \\ \bar{H}^p(j\omega) &= \frac{1}{Q}\sum_{i=1}^{Q} H_i^p(j\omega) \end{aligned} \tag{3.23}$$

It is important to recall that the primary goal of the proposed system identification approach is to derive a parameterized representation that approximates the behavior of Σ^{dyn} using a representative linear structure $\tilde{\Sigma}^{dyn}$. This approximation relies on the characterization offered by the average ETFE (23), which is computed solely based on input-output data. Considering that there existing unknown non-causal time shift, it is covenient to rewrite the average EFET:

$$\bar{H}(j\omega) = e^{j\omega t_c}\bar{H}_c(j\omega), \tag{3.24}$$

where $\bar{H}_c$ only represents the causal component of $\bar{H}$ and $e^{j\omega t_c}$ denotes the frequency-domain equivalent of the time-shift component.

The approach adopted here to derive a state-space structure from the average ETFE is based on subspace-based identification. Specifically, the method is that directly computes the associated Hankel matrices from frequency-domain data that is average EFET $\bar{H}$. Considering that non-causal shifting time t_c is unknown but it is necessary to compute the system, n iterative process to estimate the corresponding time-advance t_c are integrated with this methodology.

The approach outlined in Algorithm 2 involves several steps aimed at constructing a representative linear model for the dynamic Froude-Krylov (FK) effect. To begin, the user initiates the process by carefully selecting a suitable ensemble of multisine input signals. These input signals are designed to cover a range of relevant operating conditions that real ocean state where the device will be placed and are applied to the NLFK4ALL toolbox to collect corresponding dynamic FK output data. Once the input-output dataset is obtained, the next step involves the computation of the average empirical transfer function estimate (ETFE) using Eq.(3.13).

This average ETFE serves as a crucial base in the subsequent steps of the algorithm.

Moving forward, since the precise value of the time-advance parameter, t_c is typically unknown, a finite set of trial values, denoted as $\mathcal{T}_c$, is predefined. For each trial value in $\mathcal{T}_c$, the associated modified ETFE, denoted as $\bar{H}_c$, is computed using Eq.(3.14). Subsequently, employing subspace techniques, a corresponding approximating state-space structure, denoted as $\tilde{\Sigma}$, of an appropriate order (dimension) $\tilde{n}$ is computed. It is important to note that this computation step is encapsulated within the 'function' identify$(input, output)$.

Finally, to determine the optimal linear approximation model for the dynamic FK effect, the system $\tilde{\Sigma}_i$ that yields the lowest fitting error, along with its associated time-advance parameter t_c, is selected as the representative linear model $\tilde{\Sigma}^{dyn}$. The detailed process is shown below.

Algorithm 2 Consider the dynamic FK approximation. Assume the input set $\mathscr{U} = \{\eta_i\}_{i=1}^{Q}$ where each η_i is a carefully chosen multisine signal f_{id_i}. Define $\mathcal{T}_c = \{t_{c_i}\}_{i=1}^{P} \subset [a_l, a_h] \subset \mathbb{R}^+$ as a collection of trial time-shifts, with a_l being adequately small, and both a_h and $P \in \mathbb{N}$ being adequately large. Let $\tilde{\Sigma}$ represent an approximated state-space system, derived using an average ETFE $\bar{H}$, and characterized by a user-selected finite order (dimension) $\tilde{n}$. Additionally, let $\tilde{\mathcal{H}}$ represent the associated transfer function.

▷ Compute the set of free-surface elevation in frequency domain
$\mathscr{U} = \{\mathcal{U}_i(j\omega)\}$
▷ Compute the set of FK force in heave mode in frequency domain
$\mathscr{Y}^{dyn_z} = \left\{\mathcal{Y}_i^{dyn_z}(j\omega)\right\}$
▷ Compute corresponding average EFET in heave mode
$\bar{H}^z(j\omega) = \frac{1}{Q}\sum_{i=1}^{Q} \frac{\mathcal{Y}_i^{\mathrm{dyn_z}}(j\omega)}{\mathcal{U}_i(j\omega)}$
▷ Compute the set of FK force in pitch mode in frequency domain
$\mathscr{Y}^{dyn_p} = \left\{\mathcal{Y}_i^{dyn_p}(j\omega)\right\}$
▷ Compute corresponding average EFET in pitch mode
$\bar{H}^p(j\omega) = \frac{1}{Q}\sum_{i=1}^{Q} \frac{\mathcal{Y}_i^{\mathrm{dyn_p}}(j\omega)}{\mathcal{U}_i(j\omega)}$
for $i = 1$ to P **do**
  $T_c = t_{c_i}$
  $barH_c = e^{-j\omega T_c}\bar{H}(j\omega)$
  $\tilde{\Sigma}_i = \text{identify}\left(\bar{H}_c, \tilde{n}\right)$
  $\mathcal{E}_i = \left\|e^{j\omega T_c}\tilde{\mathcal{H}}_i(j\omega) - \bar{H}(j\omega)\right\|_2$
end for

This process ensures that the resultant model accurately captures the dynamic behavior of the system under varying operating conditions, facilitating robust analysis, simulation, and control design.

3.5 Control-oriented Model

Utilizing the suggested approximating frameworks for both static and dynamic Froude-Krylov effects, as described in Sections 3.3 and 3.4, respectively, enables the construction of a control-oriented model $\tilde{\Sigma}_W$. This model aims to approximate the nonlinear dynamics of the WEC system Σ_W as described in Eq.(3.9). To accomplish this goal, we follow the steps outlined as below.

1. Without any loss of generality, the mapping $\tilde{f}^{st}_{FK}$ representing nonlinear static FK forces within the presented approximation framework, can be 'separated' as into two parts, linear part $\tilde{f}^{\mathrm{st}}_{\mathrm{FK}_1}$ and nonlinear part $\tilde{f}^{\mathrm{st}}_{\mathrm{FK}_{\mathrm{nl}}}$:

$$\tilde{f}^{\mathrm{st}}_{\mathrm{FK}} = \tilde{f}^{\mathrm{st}}_{\mathrm{FK}} + \tilde{f}^{\mathrm{st}}_{\mathrm{FK}_{\mathrm{nl}}}, \tag{3.25}$$

where

$$\begin{aligned} \tilde{f}^{\mathrm{st}}_{\mathrm{FK}_1}(\xi) &= \begin{bmatrix} \mathcal{P}\frac{\partial \Phi}{\partial z}\Big|_{(0,0,0)} z \\ \mathcal{P}\frac{\partial \Phi}{\partial p}\Big|_{(0,0,0)} p \end{bmatrix}, \\ \tilde{f}^{\mathrm{st}}_{\mathrm{FK}_{\mathrm{nl}}}(\eta,\xi) &= \tilde{f}^{\mathrm{st}}_{\mathrm{FK}}(\eta,\xi) - \tilde{f}^{\mathrm{st}}_{\mathrm{FK}_1}(\xi), \end{aligned} \tag{3.26}$$

The linear mapping $\tilde{f}\mathrm{FK1}^{\mathrm{st}}$, emphasizing its dependence solely on ξ. According to the underlying physical principles governing WEC dynamics, it can be demonstrated that $\frac{\partial \Phi}{\partial \eta}\Big|(0,0,0) = 0$. Consequently, the linear component of the static FK force is contingent only upon the displacement of the device.

2. Regarding dynamic Froude-Krylov forces, and in alignment with the mathematical framework established for the diffraction force in Eq.(3.4), we express the output of the approximating system $\tilde{\Sigma}^{dyn}$ utilizing its corresponding impulse response function. This approach ensures consistency throughout the analysis and facilitates a comprehensive understanding of the system's dynamic behavior.

$$\tilde{f}^{\mathrm{dyn}}_{\mathrm{FK}}(\eta) = \tilde{k}^{\mathrm{dyn}}_{\mathrm{FK}} * \eta \tag{3.27}$$

where $\tilde{k}^{\mathrm{dyn}}_{\mathrm{FK}} : \mathbb{R}^+ \to \mathbb{R}^2, \tilde{k}^{\mathrm{dyn}}_{\mathrm{FK}} \in L^2(\mathbb{R})$, can be directly defined in terms of the triple of matrices (F, G, H) from Eq.(3.20) as

$$\tilde{k}^{\mathrm{dyn}}_{\mathrm{FK}}(t) = He^{F(t+t_c)}G \tag{3.28}$$

So the excitation force could be written as:

$$\mathbf{F}_{ext} = \left(\tilde{k}_{\mathrm{d}} + \tilde{k}^{\mathrm{dyn}}_{\mathrm{FK}}\right) * \eta \tag{3.29}$$

Specially there is a fundamental distinction existing between excitation force kernel utilized in linear potential flow theory models and the one proposed in this research: while $k_{\mathrm{FK}}^{\mathrm{dyn}}$ is derived here based on a representative linear model, the conventional linear potential flow theory computes the corresponding model assuming infinitesimally small motion of the device about the zero-equilibrium.

Hereafter, an overview of the framework of control-oritented model is provided, illustrating the interplay of forces in the model.

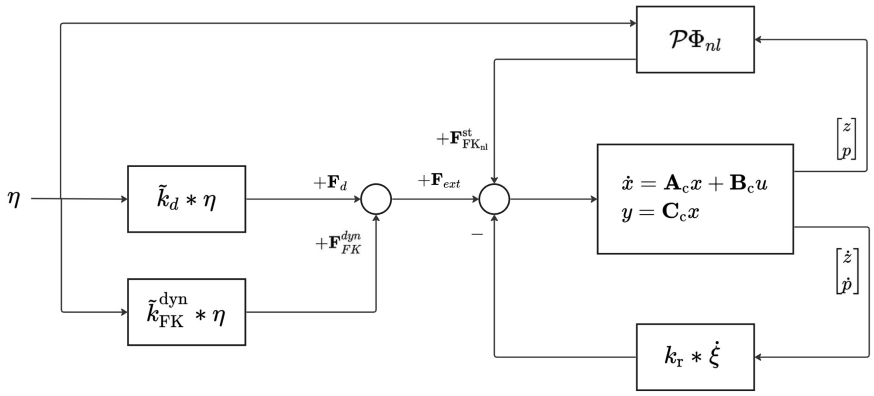

Figure 3.1: Control-oriented Model

The triple of matrices (A_c, B_c, C_c), defining used in the framework, can be straightforwardly defined as:

$$A_c = \begin{bmatrix} 0 & 0 & 1 & 0 \\ 0 & 0 & 0 & 1 \\ \frac{1}{m+A^z_\infty}\mathcal{P}_z \left.\frac{\partial \Phi}{\partial z}\right|_{(0,0,0)} & 0 & -\frac{B^z_{visc}}{m+A^z_\infty} & 0 \\ 0 & \frac{1}{I_{yy}+A^p_\infty}\mathcal{P}_p \left.\frac{\partial \Phi}{\partial p}\right|_{(0,0,0)} & 0 & -\frac{B^p_{visc}}{I_{yy}+A^p_\infty} \end{bmatrix} \tag{3.30}$$

$$B_c = \begin{bmatrix} 0 & 0 \\ 0 & 0 \\ \frac{1}{m+A^z_\infty} & 0 \\ 0 & \frac{1}{I_{yy}+A^p_\infty} \end{bmatrix} \tag{3.31}$$

$$C_c = \begin{bmatrix} 0 & 0 & 1 & 0 \\ 0 & 0 & 0 & 1 \end{bmatrix} \tag{3.32}$$

Let $x = [\xi, \dot{\xi}]^\top = [z, p, \dot{z}\dot{p}]^\top \in \mathbb{R}^4$ be the state vector associated with the WEC system, and the approximating control-oriented model can be then represented as:

$$\tilde{\Sigma}_W : \begin{cases} \dot{x} = A_c x + B_c \left(-k_\mathrm{r} * C_c x + \left(k_\mathrm{d} + k_\mathrm{FK}^\mathrm{dyn} \right) \right. \\ \qquad \left. * \eta + \mathcal{P}\Phi_{nl} \right), \\ y = C_c = \dot{\xi}, \end{cases} \tag{3.33}$$

Chapter 4

Application

4.1 Floater

The floating body employed in this research is a fundamental vertical cylinder configuration, similar with the traditional spar-buoy design commonly found in offshore applications. Notably, it exhibits distinct dynamic characteristics, featuring a significant pitch natural frequency denoted as $\omega_5 = 0.108 rad/s$. Interestingly, this frequency stands at approximately half the magnitude of its heave natural frequency, denoted as $\omega_3 = 0.216 rad/s$. This interplay between pitch and heave dynamics emphasizes the complexity inherent in the body's response to wave-induced forces and emphasizes its relevance in offshore engineering studies.

Hereafter, the values for the important parameters used in the model are listed.

Table 4.1: Physical properties of the floater

Parameter	Value
Cross section area A_C	1087 m^2
Water density ρ	1000 kg/m^3
Mass M	2.15×10^8 kg
Draft L_D	198.1 m
Gravity g	9.81 m/s^2
Constant added mass in heave mode m_3	1.37×10^7 kg
Metacentric height GM	10.1 m
Damping coefficient in heave mode C_3	1.19×10^6 kg/s
Moment of inertia in pitch modeI_5	1.12×10^{12}kgm
Distance from centre of mass to still water level L_{SC}	109.1 m
Damping coefficient in pitch mode C_5	7.54×10^9kgm/s
Constant added mass in pitch mode m_5	7.26×10^{11} kg

4.2 Excitaion Wave

To comprehensively capture the varied displacements of the floater, a multisine wave is employed for data collection. This choice enables the exploration of a wide spectrum of dynamic responses. Specifically, with natural frequencies in heave and pitch modes identified at 0.216 rad/s and 0.108 rad/s, respectively, a frequency range spanning from 0.005 rad/s to 0.3 rad/s is selected.
Recalling the fundamental insights described in Section 2.5.2, a more specific representation of multisine wave which will be utilized later is as bellow:

$$f_{\mathrm{id}}(t) = \sum_{p=1}^{K} A_p \cos\left(l_p \omega_{\mathrm{id}} t + \psi_p\right) \tag{4.1}$$

where $\{A_p, \psi_p\}_{i=1}^{K} \subset \mathbb{R}$, and where $\omega_{\mathrm{id}} = 2\pi/T_{\mathrm{id}}$, with T_{id} the measurement period, and l_p a positive integer. And the frequency ω_{id} is referred to as the fundamental frequency (in [rad/s]) of the multisine signal.

This frequency range is finely sampled at intervals of 0.001 rad/s to ensure thorough coverage so the ω_{id} is 0.001 and measurement period T_{id} is around 6284s. Additionally, to capture transient behavior effectively, simulations are conducted over 10 periods of oscillation, with a simulation time step of 1 second. This systematic approach facilitates a comprehensive understanding of the floater's behavior across various operational conditions. And the amplitude should controlled by user easily due to adapt different cases. As outlined in Section 2.5.2, in order to minimize the crest factor, Schröder phases, as defined in Eq. (2.70), are employed.

Therefore, there is an example of multisine wave used in both in time domain in Fig 4.1 and frequency domain in Fig 4.2 presented as bellow.

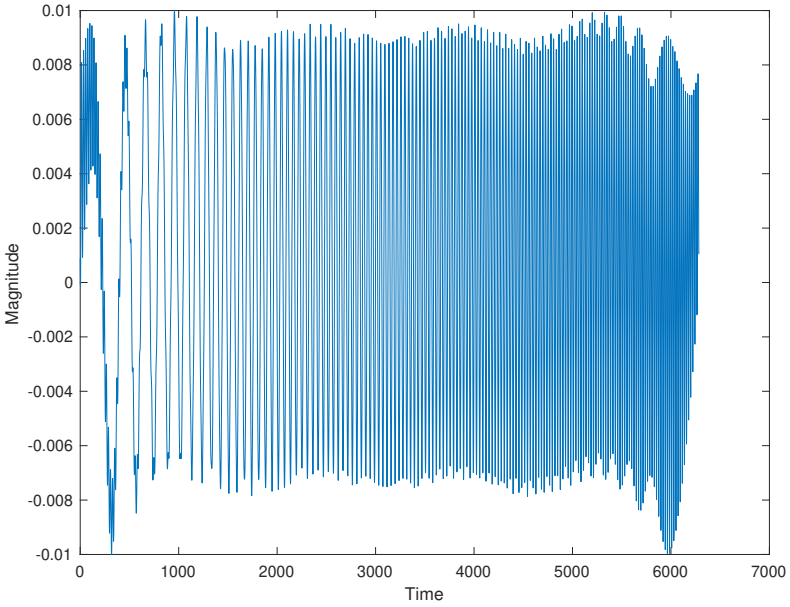

Figure 4.1: Multisine wave in time domain

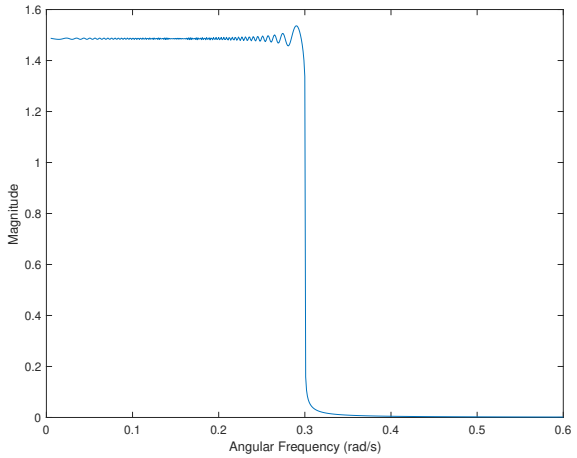

Figure 4.2: Multisine wave in frequency domain

4.3 Modelling Static FK Effect

In this study, the investigative scope is specifically limited to examining the linear aspects of the nonlinear Froude-Krylov force. This focused approach necessitates

the selection of a minimal amplitude that is sufficiently small to ensure that the behavior remains predominantly linear. Consequently, this limitation in amplitude is essential for accurately generating the values of the matrix $\mathcal{P}$, which plays an important role in the analysis. In this regard, an amplitude of 0.01 meters emerges as a reasonable choice, ensuring the requisite magnitude to effectively trigger nonlinear effects.

Recalling the procedure outlined in Algorithm 1, the initial step involves selecting suitable basis functions. These functions should effectively capture the static FK effect while mitigating the risk of overfitting, considering their intended application across various scenarios. The process entails a trial-and-error approach to determine the most suitable basis functions. After carefully considering, a set of basis functions as chosen as:

$$\Phi = \begin{bmatrix} 1 & z & p & zp & \eta & \eta p & \eta z & \eta z p \end{bmatrix}, \tag{4.2}$$

which corresponds with the first 8 terms of the polynomial series expansion of $f_{\text{FK}}^{\text{st}}$ about $(z, p, \eta) = (0,0,0)$. Using corresponding Algorithm 2, the final computed solution of $\mathcal{P}$ is:

$$\begin{bmatrix} -517.273244940658 & -9021.61694855900 \\ -10788572.2726150 & -22249386712.3616 \\ -10702584.2812758 & -392855.737666598 \\ 35105784.4688144 & 1345866867.70791 \\ 598401.682233837 & 10108894.2575522 \\ -18229978.9275238 & -1925148668.90044 \\ -335277.035124412 & 3025192.00161225 \\ -14798543922.6449 & 460249872338.523 \end{bmatrix} \tag{4.3}$$

4.4 Modelling Dynamic FK Effect

Now that we have outlined the approximation of static nonlinear FK forces using the proposed framework, we advance towards the modeling of dynamic FK effects tailored for control purposes. This progression aligns with the systematic approach delineated in Section 3.3, delineated by Algorithm 2.

Prior to the implementation of this procedure, it is important to carefully select an appropriate excitation multisine wave. This selection process aims to ensure that the resulting Bode diagram of dynamic Froude-Krylov forces exhibits a notably smooth profile across the designated frequency spectrum. Specifically, the chosen frequency range spans from 0 rad/s to 0.25 rad/s, thereby encompassing the natural frequencies associated with both heave and pitch modes.

Here are some resulting Bode diagrams from Fig 4.3 to Fig 4.6. In each figure, the upper two plots depict the behavior in the heave mode, while the lower two plots represent the pitch mode.

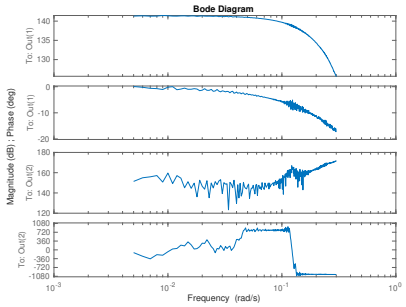

Figure 4.3: Amplitude-2m

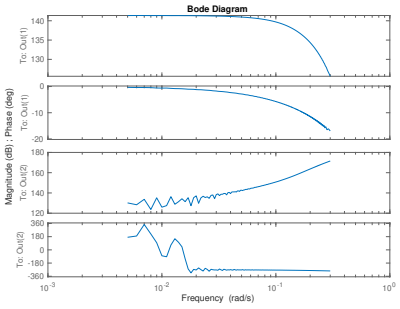

Figure 4.4: Amplitude-0.1m

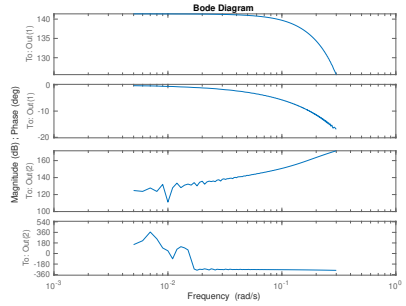

Figure 4.5: Amplitude-0.05m

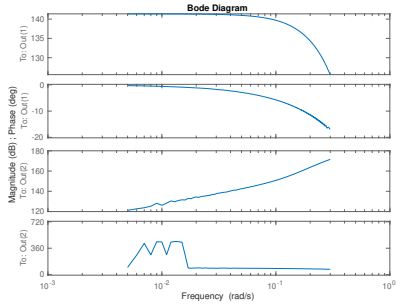

Figure 4.6: Amplitude-0.01m

Therefore, the multisine wave selected has the amplitude as 0.01 meters.

Regarding the specific parameters characterizing Algorithm 2, the order (dimension) is set to $\tilde{n}$=10, which strikes a balance between computational complexity and model accuracy. The set of uniformly spaced trial time-shifts $\mathcal{T}_c$, used to compute an estimate of the output time-advance characterizing the dynamic FK system, is defined such that $\mathcal{T}_c \in [0,15]$. As depicted in Fig 4.7, illustrating the approximation error of Algorithm 2 across different T_c values, the optimal time-advance is determined to be t_c=6.32s.

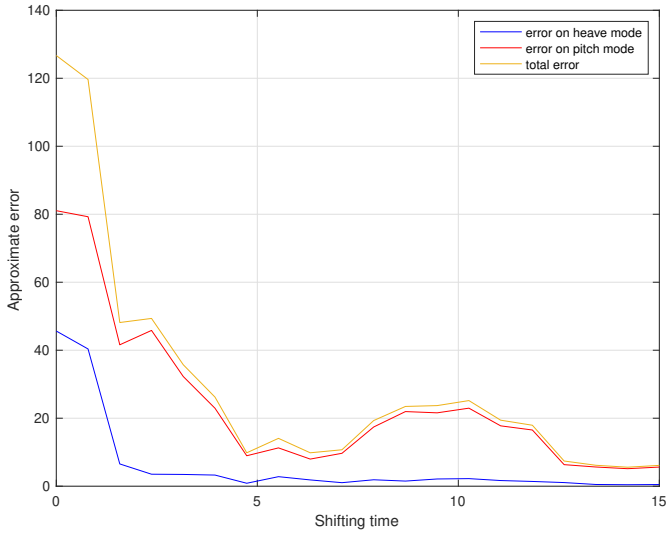

Figure 4.7: Approximation error of different shifting time

The outcomes of implementing the proposed algorithm are synthesized in the Fig 4.8 where the upper two subplots are for heave mode and the down two subplots are for pitch mode, representing by a comprehensive Bode plot. This plot composes an averaged ETFE $\bar{\mathrm{H}}(j\omega)$ (depicted in orange lines), and the frequency-response mapping linked with the computed approximate model $\tilde{\Sigma}_{dyn}$ (displayed in yellow lines). This figure distinctly demonstrates a fairly promising alignment with the target $\bar{\mathrm{H}}(j\omega)$, which mean it is a robust fit. Moreover, to emphasize the difference between conventional linear hydrodynamic FK representations and the innovative approach, this figure depicts the frequency-response of the linear dynamic FK model derived via BEM solvers (specifically, Nemoh in this context).

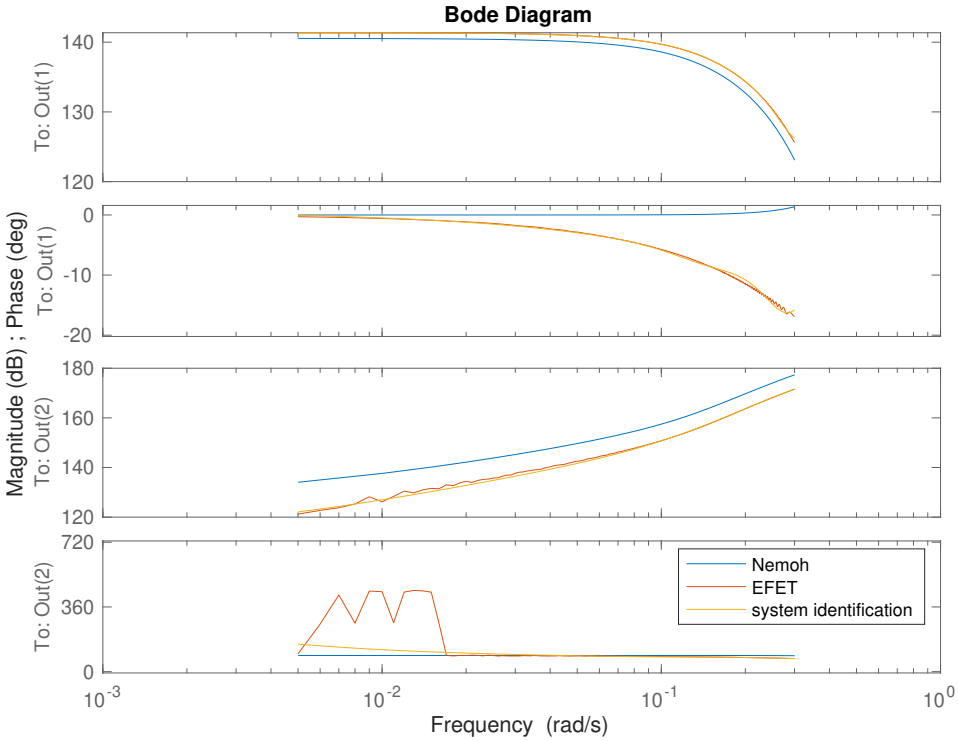

Figure 4.8: Bode plot of the corresponding average ETFE, computed approximating model, and linear BEM model

It's important to note a significant gap between the linear BEM model which is Nemoh in this case and the representative linear structure derived from Algorithm 2, in terms of both amplitude and phase descriptions, especially the phase one. Specifically, the BEM model fails to capture the time-advance adequately, resulting in almost zero-phase behavior within the frequency range relevant to the device's operational conditions. This discrepancy in phase representation could lead to notable shortcomings in energy-maximizing performance for controllers relying on dynamic FK BEM models. This is because having accurate insight into the instantaneous phase of the WEC system variables is crucial for achieving satisfactory control performance.

To comprehensively assess the quality of the combined static and dynamic Froude-Krylov approximation models, we present a detailed comparison in Fig 4.9. This comparison involves the target static and dynamic FK force, denoted as $\mathcal{Y}^z_{FK_{st}}$, $\mathcal{Y}^p_{FK_{st}}$, $\mathcal{Y}^z_{FK_{dy}}$ and $\mathcal{Y}^p_{FK_{dy}}$, which are computed using the nonlinear solver

NlFK4All, and the corresponding approximation obtained through the proposed control-oriented framework, denoted as $\tilde{\mathcal{Y}}^z_{FK_{st}}$, $\tilde{\mathcal{Y}}^p_{FK_{st}}$, $\tilde{\mathcal{Y}}^z_{FK_{dy}}$ and $\tilde{\mathcal{Y}}^p_{FK_{dy}}$. At the top of this figure, there is a visual representation of the time traces associated with the target $\mathcal{Y}^z_{FK_{st}}$, $\mathcal{Y}^p_{FK_{st}}$, $\mathcal{Y}^z_{FK_{dy}}$ and $\mathcal{Y}^p_{FK_{dy}}$(indicated by dotted lines) and the approximating $\tilde{\mathcal{Y}}^z_{FK_{st}}$, $\tilde{\mathcal{Y}}^p_{FK_{st}}$, $\tilde{\mathcal{Y}}^z_{FK_{dy}}$ and $\tilde{\mathcal{Y}}^p_{FK_{dy}}$(depicted by solid lines) Froude-Krylov forces. This comparison enables a direct observation of how well the approximating model aligns with the target FK force over time.
Furthermore, Fig 4.10 offers a quantitative measure of the approximation error. This error is computed as the difference between the target and approximating total FK forces, normalized by the maximum absolute value of the target force. By consistently evaluating this approximation error, we can evaluate the performance of our proposed approximation framework.

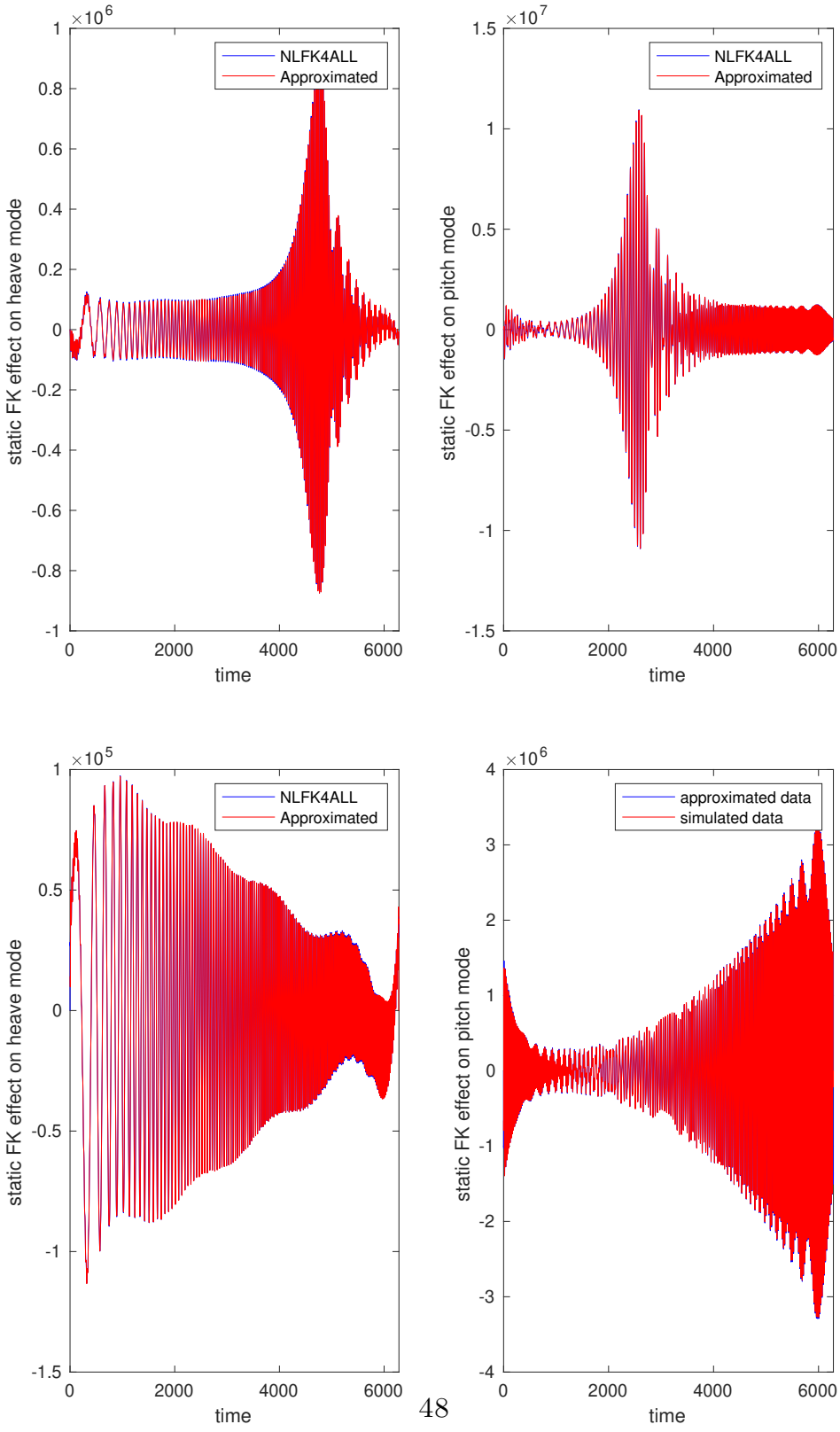

Figure 4.9: Time-traces corresponding with target and approximating total FK force

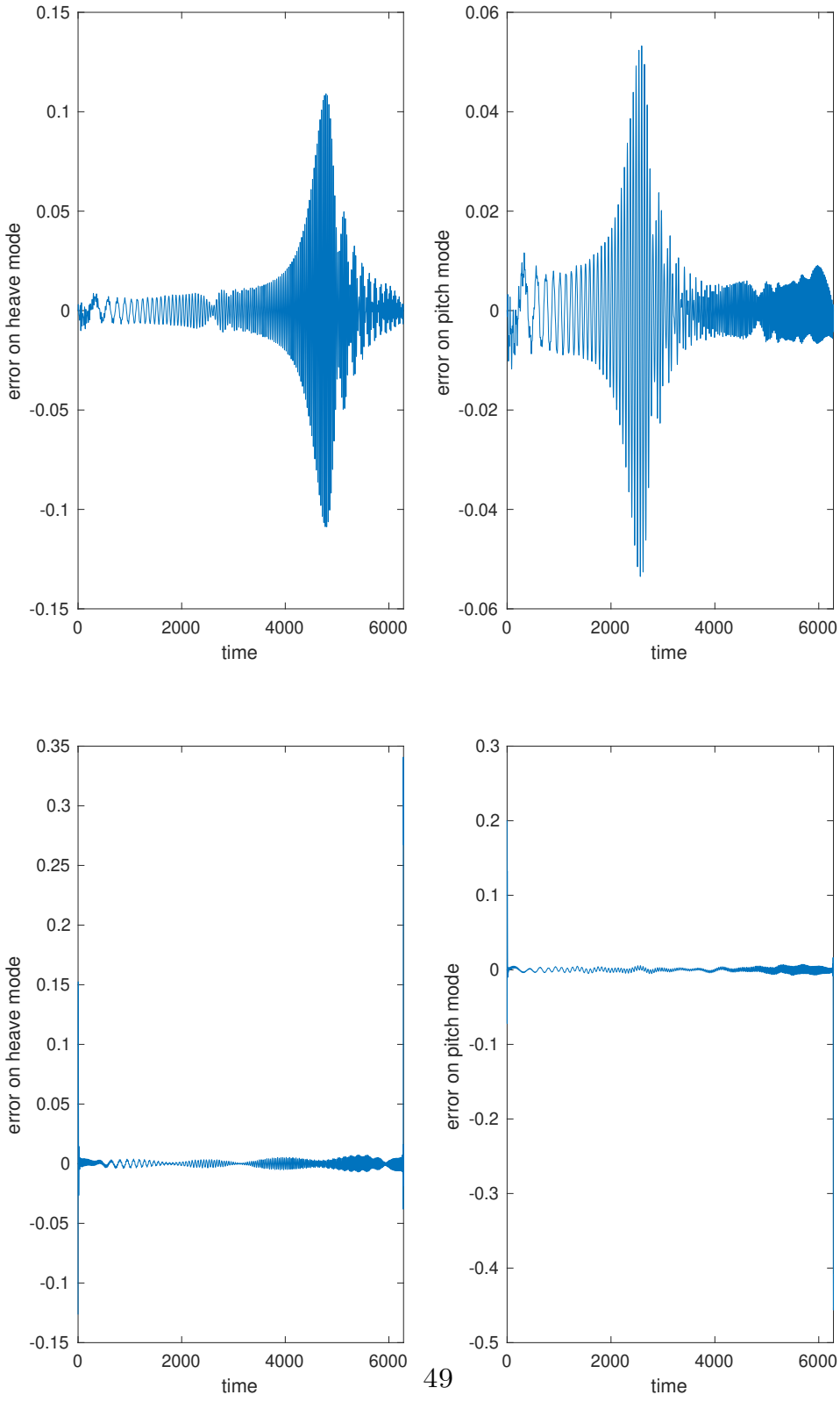

Figure 4.10: Time-traces of associated approximation error

In essence, these figures not only presents empirical data but also serves as a gateway to understanding the behavior of the system under consideration. Overall, this comprehensive analysis shows the efficacy of this approach in accurately approximating the total FK force, thus highlighting the practical utility and reliability of the control-oriented modeling strategy.

4.5 Building Control-oriented Model

Following the development of models to approximate both static and dynamic Froude-Krylov effects, these models are integrated into the control-oriented framework. The figure below Fig 4.11 illustrates the displacement(heave and pitch in this cotext) of the floater computed by the numerical solver NLFK4ALL alongside the control-oriented model proposed in this research.

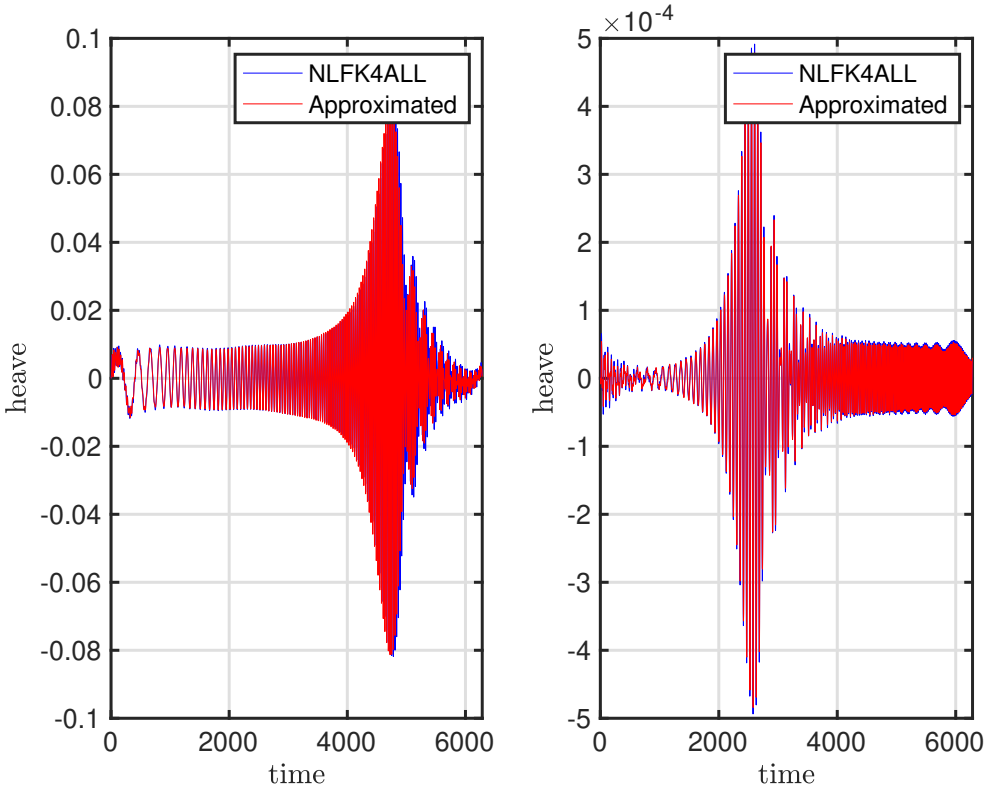

Figure 4.11: Displacemnt comparation between NLFK4ALL and proposed framework

The image shown in Fig 4.11 effectively demonstrates how well the proposed framework works. By carefully combining models of both static and dynamic Froude-Krylov effects into a unified system that focuses on control, this computational approach accurately represents the movements of the floater. The comparison in the figure highlights that the model's calculations of the floater's movements are as accurate as those from a numerical solver, NLFK4ALL, while also emphasizing that the proposed method requires less computational effort. This observation points out that the framework is designed to handle complex calculations efficiently and provide precise results about the floater's behavior.

4.6 Validation

4.6.1 Jonswap excitation wave

For the validation of the developed model, a Jonswap wave profile is employed to emulate a realistic sea state. The JONSWAP (Joint North Sea Wave Project) spectrum is particularly chosen due to its ability to closely represent the spectral characteristics observed in natural sea states. It adjusts the peak enhancement factor to simulate varying sea state conditions more accurately than other models. The wave profile is characterized by a significant wave height of 0.1 meters and a period of 54 seconds. The frequency range of the wave, spanning from 0.09 rad/s to 0.21 rad/s, comprehensively covers the natural frequencies of the floater in both heave and pitch modes. This selection ensures that the wave conditions used in the model testing are representative of the operational environment anticipated for the device. The figure below Fig 4.12 illustrates the magnitude of this wave in the frequency domain, providing a visual representation of the wave characteristics used for model validation.

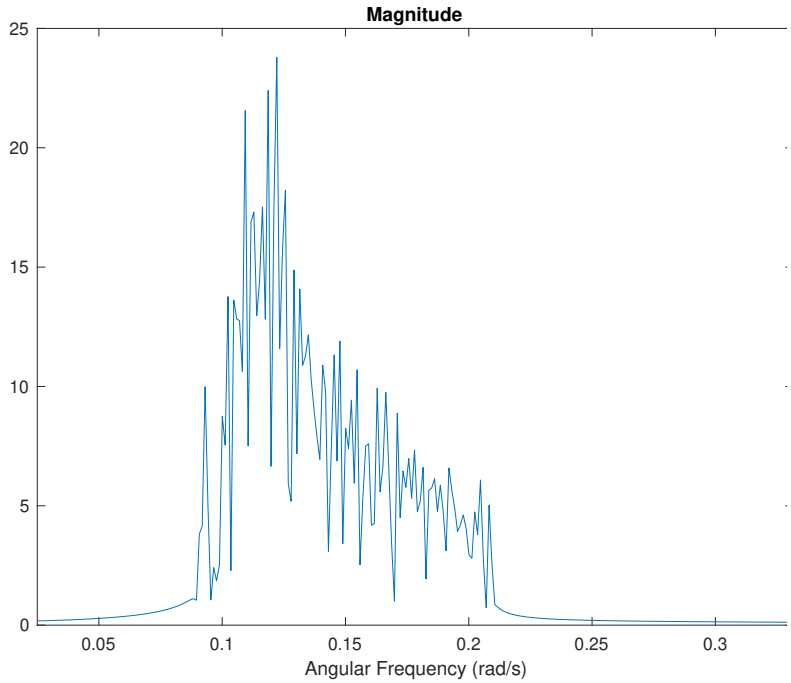

Figure 4.12: Jonswap wave in frequency domain

4.6.2 Static FK Effect Validation

Initially, it is essential to make sure the adequacy of the developed model intended to approximate the static Froude-Krylov force, ensuring its suitability for further analysis. The results from this preliminary validation are crucial for proceeding confidently with subsequent modeling stages.

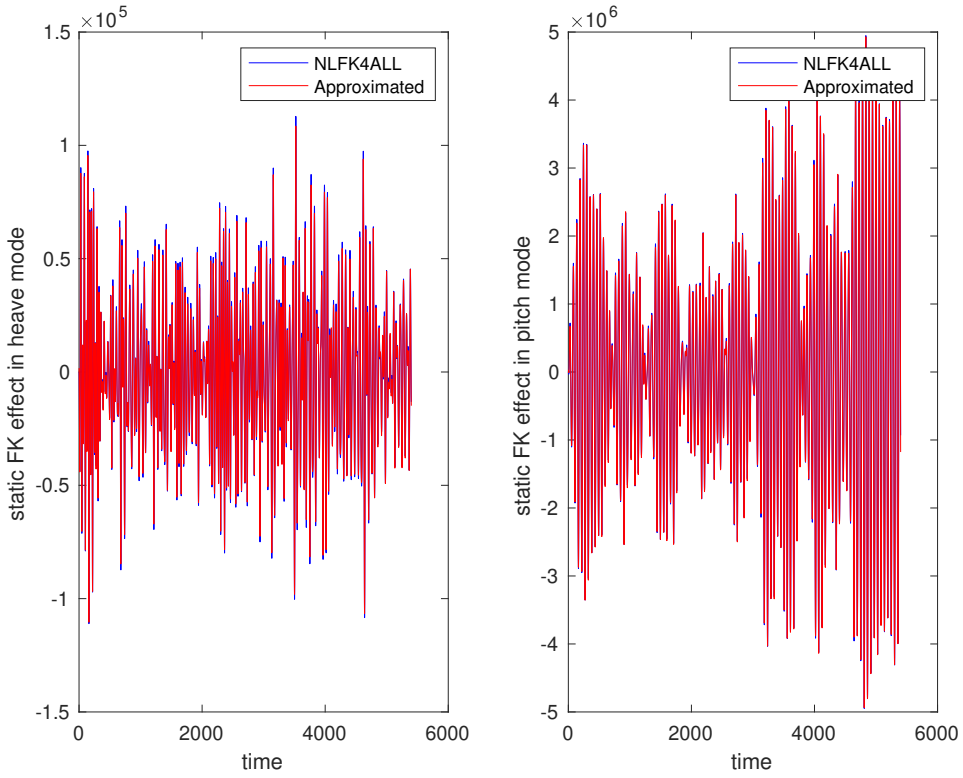

Figure 4.13: Static FK effect compararion in Jonswap wave

The findings, as depicted in the accompanying figure, indicate that the model demonstrates a high degree of accuracy in approximating the static Froude-Krylov force. The alignment between the model's predictions and the empirical data suggests that the model not only captures the fundamental dynamics with considerable precision but also exhibits robustness in its predictive capabilities.

4.6.3 Dynamic FK Effect Validation

Secondly, it is important to evaluate the fidelity with which the dynamic Froude-Krylov effects are approximated. An examination of the accompanying figure reveals that the approximated dynamic Froude-Krylov force is consistently larger than that derived from the NLFK4ALL solver. Notably, this discrepancy manifests as an error that is changing with magnitude constantly across the entire range of time. This systematic deviation is attributed to the inherent nonlinearity introduced by the multisine wave employed during the identification process, a characteristic not encapsulated by the Jonswap spectrum typically used.

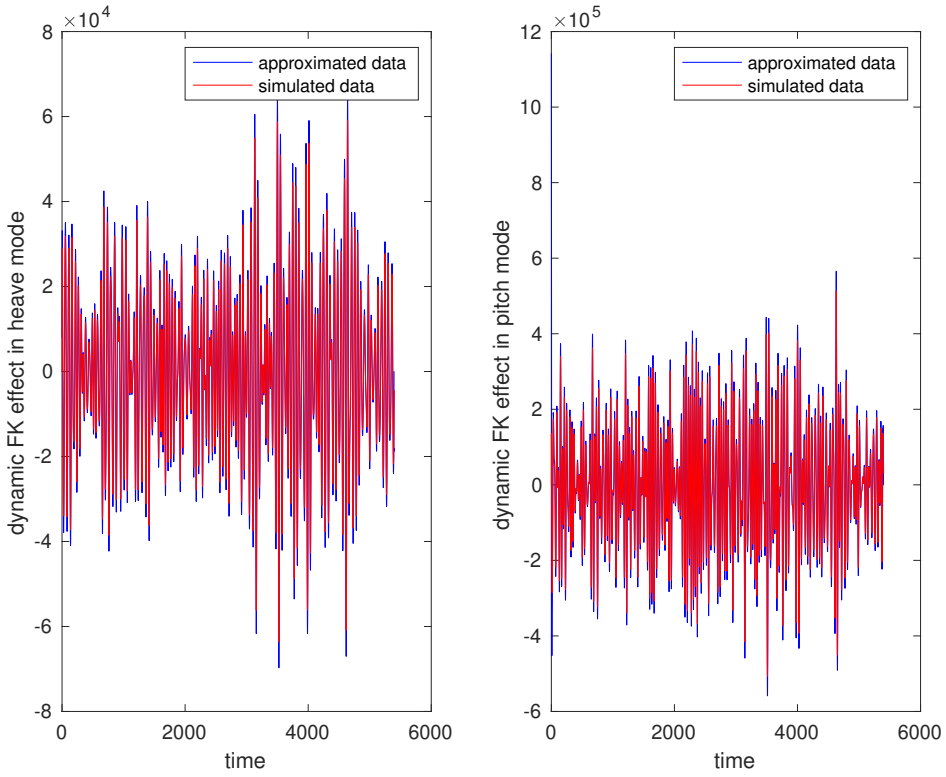

Figure 4.14: Dynanic FK effect compararion in Jonswap wave

To address and mitigate this observed deviation, a scaling coefficient of 0.917 is applied to the approximated dynamic Froude-Krylov effect. This adjustment significantly enhances the alignment between the approximated results and the target data derived from NLFK4ALL, as demonstrated in the subsequent figure.

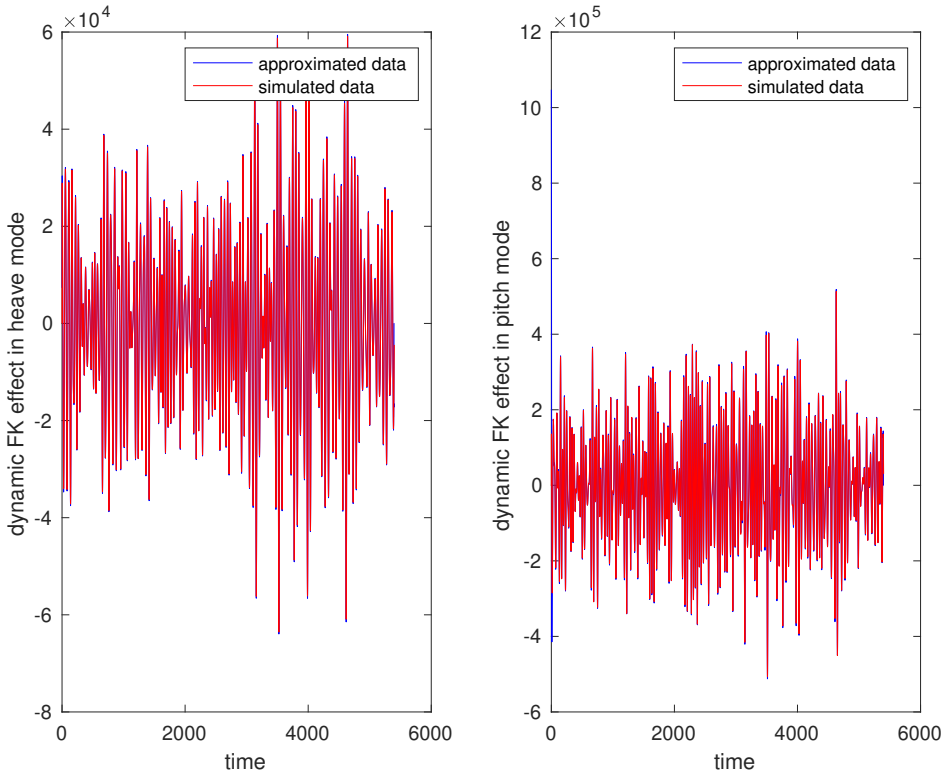

Figure 4.15: Dynanic FK effect compararti̇on in Jonswap wave after scaling

The introduction of this scaling factor effectively normalizes the response, ensuring that the approximated and actual dynamic Froude-Krylov forces align closely across the tested conditions. This alignment is critical for validating the accuracy of the modeling approach and shows the adaptability of our methodology in compensating for the nonlinear influences encountered during the wave identification phase.

This rigorous assessment and correction process not only affirms the validity of the approximated model but also illustrates the analytical necessary to refine and adapt hydrodynamic models to accurately reflect complex real-world phenomena.

4.6.4 Validation of Control-oriented Model

Following the successful validation of both static and dynamic Froude-Krylov force components, the next logical step in our research is to proceed with the validation of the entire model that simulates the displacement of the floater.

The accompanying figure presents the results of this extensive model validation. It illustrates how the model performs in approximating the floater's displacement, focusing on the pitch and heave modes in this context.

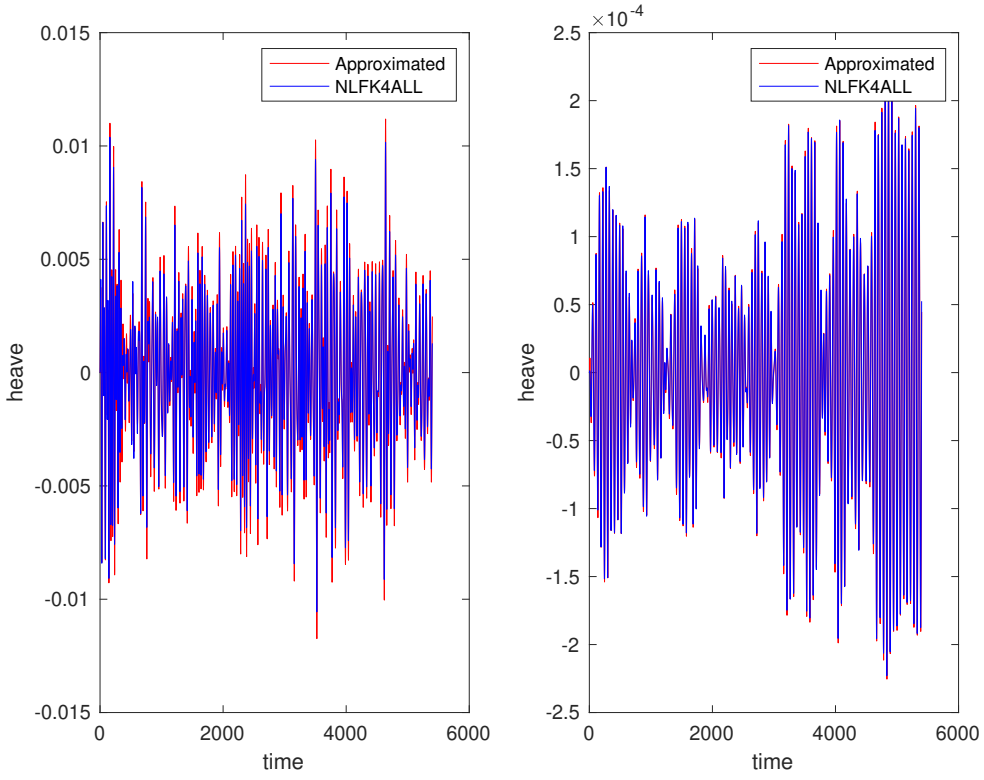

Figure 4.16: Displacement comparation in Jonswap wave

In the pitch mode, the model demonstrates a quite good level of accuracy, closely replicating the expected displacements. However, the approximation in heave mode, while generally good, does not achieve the same level of precision. This discrepancy indicates potential areas for refinement in how the model handles vertical displacements or interacts with wave forces in heave mode.

Chapter 5

Conclusion

In this Master's thesis, the focus has been on the data-based modeling of nonlinear hydrodynamics that Froude-Krylov effect in this scope for wave energy conversion systems. The primary objective was to develop accurate models that capture the complex nonlinear behavior of wave energy converters, with the ultimate goal of enhancing their performance and efficiency, and at the same time suitable for developing control system on the basis of it.

It begins with highlighting the importance of nonlinear dynamics in accurately predicting device performance. The significance of the Froude-Krylov effect and other nonlinearities in WEC modeling was emphasized, indicating the necessity to account for these factors to optimize design and control strategies.

This Master's thesis has tried to extend the boundaries of knowledge in the field of wave energy conversion, building upon the foundational work of my supervisor Niclas Feado and Giuseppe Giorgi. The goal of this study was to expand upon the existing data-based modeling approach for wave energy converters, initially developed for single degree of freedom systems, and extend it to encompass the complexities of two degrees of freedom systems. This extended framework enabled the exploration of more complex interactions between wave conditions and WEC behavior, yielding valuable insights into system performance across different scenarios.

The challenges of balancing modeling accuracy with computational efficiency were also addressed, which involved in developing complex models for real-time applications. The need for efficient computation and accurate mathematical models in design processes was highlighted.

Through the exploration of nonlinear hydrodynamics and the implementation of advanced modeling techniques, this thesis has contributed to a deeper understanding of wave energy conversion systems. The insights gained from this research have practical implications for the design, optimization, and control of WECs, offering new path for improving their efficiency and reliability.

As the wave energy industry continues to evolve, the work of this thesis pave

the way for further research and development in the field of wave energy conversion. By continuing to refine data-based models and explore innovative solutions, it is possible to drive advancements in wave energy technology and accelerate the transition towards a more sustainable energy future.

In conclusion, this Master's thesis represents a significant step towards exploiting the full potential of wave energy conversion systems through the modeling of nonlinear hydrodynamics. The work presented here lays the groundwork for future advancements in the field, with the hope of contributing to the widespread adoption of wave energy as a clean and renewable energy source.

Bibliography

[1] Mehmet Melikoglu. «Current status and future of ocean energy sources: A global review». In: *Ocean Engineering* 148 (2018), pp. 563–573 (cit. on p. 1).

[2] EMEC. *Wave devices*. Mar. 2024. URL: `https://www.emec.org.uk/marine-energy/wave-devices/` (cit. on p. 1).

[3] Guang Li, George Weiss, Markus Mueller, Stuart Townley, and Mike R Belmont. «Wave energy converter control by wave prediction and dynamic programming». In: *Renewable energy* 48 (2012), pp. 392–403 (cit. on p. 2).

[4] Antonio F de O Falcao. «Wave energy utilization: A review of the technologies». In: *Renewable and sustainable energy reviews* 14.3 (2010), pp. 899–918 (cit. on p. 2).

[5] Yong Cheng, Chen Xi, Saishuai Dai, Chunyan Ji, Maurizio Collu, Mingxin Li, Zhiming Yuan, and Atilla Incecik. «Wave energy extraction and hydroelastic response reduction of modular floating breakwaters as array wave energy converters integrated into a very large floating structure». In: *Applied Energy* 306 (2022), p. 117953 (cit. on p. 3).

[6] Giuseppe Giorgi. *Nonlinear hydrodynamic modelling of wave energy converters under controlled conditions*. National University of Ireland, Maynooth (Ireland), 2018 (cit. on pp. 3, 4).

[7] Jennifer Van Rij, Yi-Hsiang Yu, Alan McCall, and Ryan G Coe. «Extreme load computational fluid dynamics analysis and verification for a multibody wave energy converter». In: *International Conference on Offshore Mechanics and Arctic Engineering*. Vol. 58899. American Society of Mechanical Engineers. 2019, V010T09A042 (cit. on p. 3).

[8] Malin Göteman, Marianna Giassi, Jens Engström, and Jan Isberg. «Advances and challenges in wave energy park optimization—a review». In: *Frontiers in Energy Research* 8 (2020), p. 26 (cit. on p. 3).

[9] Nicolás Faedo, Sébastien Olaya, and John V Ringwood. «Optimal control, MPC and MPC-like algorithms for wave energy systems: An overview». In: *IFAC Journal of Systems and Control* 1 (2017), pp. 37–56 (cit. on p. 3).

[10] Nicolás Faedo, G Giorgi, JV Ringwood, and Giuliana Mattiazzo. «Optimal control of wave energy systems considering nonlinear Froude–Krylov effects: control-oriented modelling and moment-based control». In: *Nonlinear Dynamics* 109.3 (2022), pp. 1777–1804 (cit. on pp. 3, 5).

[11] Tania Demonte Gonzalez, Gordon G Parker, Enrico Anderlini, and Wayne W Weaver. «Sliding mode control of a nonlinear wave energy converter model». In: *Journal of Marine Science and Engineering* 9.9 (2021), p. 951 (cit. on p. 4).

[12] Isha Malekar. «Nonlinear model predictive control of wave energy converter». In: (2021) (cit. on p. 4).

[13] Giuseppe Giorgi and John V Ringwood. «Computationally efficient nonlinear Froude–Krylov force calculations for heaving axisymmetric wave energy point absorbers». In: *Journal of Ocean Engineering and Marine Energy* 3 (2017), pp. 21–33 (cit. on pp. 4, 29).

[14] Sung-Jae Kim, Weoncheol Koo, and Moo-Hyun Kim. «The effects of geometrical buoy shape with nonlinear Froude-Krylov force on a heaving buoy point absorber». In: *International Journal of Naval Architecture and Ocean Engineering* 13 (2021), pp. 86–101 (cit. on p. 4).

[15] Ye Li and Yi-Hsiang Yu. «A synthesis of numerical methods for modeling wave energy converter-point absorbers». In: *Renewable and Sustainable Energy Reviews* 16.6 (2012), pp. 4352–4364 (cit. on p. 5).

[16] G Giorgi. «Nonlinear Froude–Krylov Matlab Demonstration Toolbox». In: *OpenWave Politecnico di Torino: Turin, Italy* (2019) (cit. on p. 5).

[17] International Electrotechnical Commission et al. «Marine energy–Wave, tidal and other water current converters–Part 2: Design requirements for marine energy systems». In: *International Electrotechnical Commission: Geneva, Switzerland* (2016) (cit. on pp. 25, 26).

[18] T Kimpián and F Augusztinovicz. «Multiphase multisine signals–Theory and practice». In: *Proceedings of ISMA2016 including USD* (2016), pp. 19–21 (cit. on p. 26).